AGU PUBLICATIONS

JGR

Journal of Geophysical Research: Oceans

RESEARCH ARTICLE

10.1002/2013JC009779

Forcing mechanisms of intraseasonal SST variability off central Peru in 2000–2008

Serena Illig[1,2], Boris Dewitte[1], Katerina Goubanova[1], Gildas Cambon[1], Julien Boucharel[3], Florian Monetti[2], Carlos Romero[2], Sara Purca[2], and Roberto Flores[2]

[1]Laboratoire d'Etudes en Géophysique et Océanographie Spatiale, CNRS/IRD/UPS/CNES, Toulouse, France, [2]Instituto del Mar del Peru, Callao, Peru, [3]Department of Meteorology, University of Hawaii at Manoa, Honolulu, Hawaii, USA

Key Points:
- Remote equatorial forcing accounts for ~20% of the intraseasonal SST regime
- The wind-SST relationship is modulated seasonally by the mean stratification
- Coastal SST variability results from advection and mixing processes

Supporting Information:
- Supporting text and figures

Correspondence to:
Serena Illig,
illig@legos.obs-mip.fr

Citation:
Illig, S., B. Dewitte, K. Goubanova, G. Cambon, J. Boucharel, F. Monetti, C. Romero, S. Purca, and R. Flores (2014), Forcing mechanisms of intraseasonal SST variability off central Peru in 2000–2008, *J. Geophys. Res. Oceans*, *119*, doi:10.1002/2013JC009779.

Received 31 DEC 2013
Accepted 1 MAY 2014
Accepted article online 10 MAY 2014

Abstract The Sea Surface Temperature (SST) intraseasonal variability (40–90 days) along the coast of Peru is commonly attributed to the efficient oceanic connection with the equatorial variability. Here we investigate the respective roles of local and remote equatorial forcing on the intraseasonal SST variability off central Peru (8°S–16°S) during the 2000–2008 period, based on the experimentation with a regional ocean model. We conduct model experiments with different open lateral boundary conditions and/or surface atmospheric forcing (i.e., climatological or not). Despite evidence of clear propagations of coastal trapped waves of equatorial origin and the comparable marked seasonal cycle in intraseasonal Kelvin wave activity and coastal SST variability (i.e., peak in Austral summer), this remote equatorial forcing only accounts for ~20% of the intraseasonal SST regime, which instead is mainly forced by the local winds and heat fluxes. A heat budget analysis further reveals that during the Austral summer, despite the weak along-shore upwelling (downwelling) favorable wind stress anomalies, significant cool (warm) SST anomalies along the coast are to a large extent driven by Ekman-induced advection. This is shown to be due to the shallow mixed layer that increases the efficiency by which wind stress anomalies relates to SST through advection. Diabatic processes also contribute to the SST intraseasonal regime, which tends to shorten the lag between peak SST and wind stress anomalies compared to what is predicted from an advective mixed-layer model.

1. Introduction

The west coast of South-America hosts a very productive oceanic ecosystem [*Carr*, 2002] that is primarily due to the upwelling conditions that bring nutrient-enriched waters from the subthermocline to the surface, enabling an intense primary production. The upwelling conditions are driven by Ekman dynamics from the prevailing equatorward along-shore mean winds that generally occur in eastern boundary current systems [*Bakun*, 1990]. In the Humboldt system, along the coasts of Peru and Chile, the upwelling is highly variable due to the influence of the large scale circulation of the Pacific Ocean. For instance, at interannual time scales, El Niño Southern Oscillation (ENSO) has been shown to influence the upwelling off Peru [*Colas et al*., 2008; *Dewitte et al*., 2012] and Chile [*Pizarro et al*., 2002; *Vega et al*., 2003] through oceanic teleconnections. ENSO atmospheric teleconnections have also been shown to drive anomalous upwelling conditions off Central Chile [*Montecinos and Gomez*, 2010; *Goubanova et al*., 2011; *Rahn*, 2012], whereas off Peru, they are more ubiquitous [*Goubanova et al*., 2011]. Most studies on upwelling variability in the Humboldt system and its connection with the equatorial variability have focused on the analysis of coastal sea level and current (cf. *Pizarro et al*. [2001, 2002], *Ramos et al*. [2006], *Dewitte et al*. [2008b], *Vega et al*. [2003], and *Ramos et al*. [2008] for the seasonal to interannual time scales and *Brink* [1982], *Enfield* [1987], *Spillane et al*. [1987], *Shaffer et al*. [1997], *Clarke and Ahmed* [1999], *Hormazabal et al*. [2002], *Camayo and Campos* [2006], and *Belmadani et al*. [2012] for the intraseasonal time scales). Very few studies have investigated the variability of the Sea Surface Temperature (SST) although it is often used as a main indicator for upwelling variability [*Demarcq and Faure*, 2000] and for marine resource management.

Whereas during extreme El Niño events, coastal SST warms off Peru and Northern Chile due to the impact of the strong downwelling equatorial Kelvin wave [*Dewitte et al*., 2012], at intraseasonal time scales, the equatorial connection for SST is more ambiguous due in part to the weaker amplitude of the intraseasonal Kelvin wave. The SST intraseasonal variability off Peru may be also forced by local winds that relates to a large extent with the variability of the South Pacific Anticyclone [*Dewitte et al*., 2011]. This dual forcing is

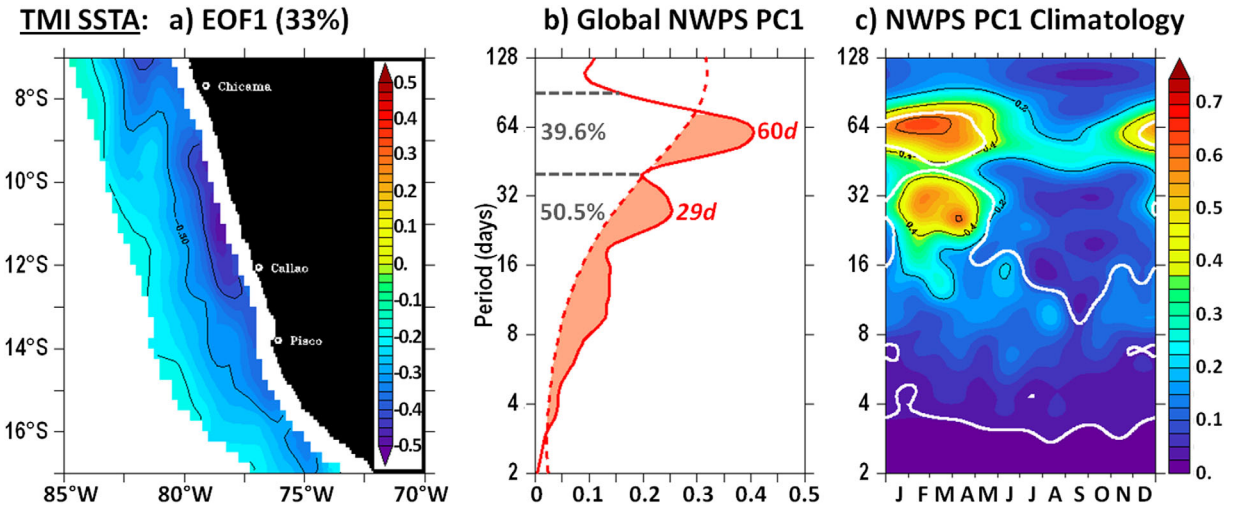

Figure 1. Dominant mode of the Empirical Orthogonal Function (EOF) analysis of the observed satellite TMI-OI daily subseasonal SST anomalies (SSTA, cf. section 2 for data and filtering descriptions) that captures 33% of the variance. (a) Spatial pattern (color, in °C). (b) Global Normalized Wavelet Power Spectrum (NWPS) of nondimensional PC1-SSTA (period is in days). Dashed line indicates the 95% confidence level and shading underlines significant global NWPS. (c) A 8 year climatology of the NWPS estimated over the period June 2000 to May 2008. White line shows the 95% confidence level.

reflected in the spectrum of the SST along the coast. The Figure 1 shows the dominant pattern of variability of the subseasonal (namely ~2–120 days) SST off central Peru during the 2000–2008 period. The dominant mode of SST subseasonal anomalies off central Peru (Figure 1a) consists in a meridionally extended narrow coastal fringe of SST anomalies with amplitudes decreasing from the coast to the offshore ocean, with maximum amplitudes of anomalies with absolute values larger than 0.4°C located at 11°S. This SST mode governs the coastal SST variability along the coast of central Peru since the associated SST anomalies averaged within the 200 km coastal band between 16°S and 8°S explains ~82% of the satellite coastal subseasonal variability. The dominant time scales of variability of the time series associated with this mode (PC1-SSTA) can be separated into two regimes (Figure 1b), a high-frequency subseasonal regime that corresponds to the 2–40 day^{-1} frequency band (accounting for 50% of the total power of the PC1-SSTA spectrum) and a low-frequency subseasonal regime (hereafter referred to as intraseasonal regime) that corresponds to the 40–90 day^{-1} frequency band and that represents 40% of the total power of the PC1-SSTA spectrum. Whereas the high-frequency regime can be undoubtedly related to synoptically forced winds, particularly active in Austral winter, *Dewitte et al*. [2011] were not able to characterize the forcing mechanism of the intraseasonal regime, although noting a comparable marked seasonal dependence of the Intraseasonal Equatorial Kelvin Wave (IEKW) and the SST along the coast that peaks in Austral summer (from December to May, see the climatological wavelet spectrum in Figure 1c). However, their analysis was limited by the observed data sets at their disposal. In particular, due to the extended masking of the satellite data near the coast, the identification of the signature of the Coastal Trapped Waves (CTW) on the SST remains difficult. Also, the scarcity of subsurface observations prevents the investigation of the thermocline variability that should reveal the equatorial connection more clearly [*Brink*, 1982]. Here we extend the study by *Dewitte et al*. [2011] based on satellite observations with the objective of (1) determining the processes associated with the SST variability along the coast of Peru within the intraseasonal regime (namely 40–90 days) and (2) resolving the issue of the forcing of this SST variability by the equatorial Kelvin wave. Besides the societal concern in relation with marine resource management, the issue of the forcing of the SST variability at intraseasonal time scales off Peru is also worth tackling in order to better understand the air-sea interactions in upwelling systems (e.g., VOCALS project [*Mechoso et al*., 2013]).

Our approach is based on the experimentation with a regional ocean model which allows overcoming the limitations encountered by *Dewitte et al*. [2011] as well as providing a quantitative evaluation of the mixed-layer processes associated with the upwelling intraseasonal variability. The focus is on the 2000–2008 period benefiting from the QuickSCAT winds that have been used previously for regional modeling studies in this region [*Penven et al*., 2005; *Montes et al*., 2010]. Within this model setup, our results indicate that SST

variability at intraseasonal time scales off central Peru over this period is only marginally influenced by the equatorial Kelvin wave and results mostly from wind forcing despite its very weak variability. The paper then documents the mixed-layer processes associated with this peculiar SST intraseasonal regime highlighting the contribution of mixing processes and its coupling with diabatic forcing.

The paper is structured as follows: section 2 details the observed data sets and the global reanalysis, as well as the methodology used in this study. Section 3 introduces the regional oceanic model and its validation against in situ and satellite data and further describes the various numerical experiments carried out. Section 4 is devoted to the evaluation of the relative contribution of local wind and remote equatorial Kelvin wave to the intraseasonal SST variability off Peru. In section 5, a heat budget of the mixed-layer documents the processes by which local atmospheric forcing triggers intraseasonal SST variability. Finally, a discussion of the results followed by concluding remarks and perspectives to this work are given in section 6.

2. Data and Methods

We use satellite data, along with reanalysis outputs for the forcing of the model simulations. Other data sets are used for the validation, and those are presented in Appendix A.

2.1. Satellite Observations

2.1.1. Wind Stress

The near-surface atmospheric circulation over the ocean is described through daily zonal and meridional wind stress components from the NASA satellite QuikSCAT. Homogeneous temporal series of daily mean wind stress fields, on global $0.5^\circ \times 0.5^\circ$ resolution grids, are generated from L2B product (distributed by JPL/PO.DAAC) by the French ERS Processing and Archiving Facility CERSAT (http://www.ifremer.fr/cersat/en/data/overview/gridded/mwfqscat.html). Note that in near-coastal region due to land contamination QuikSCAT wind stress data are masked and are not available within 25 km off the coast.

2.1.2. SST

Estimates of SST were obtained from the Tropical Rainfall Measuring Mission (TRMM [*Kummerow et al*., 2000]) Microwave Imager (TMI) produced by Remote Sensing Systems (RSS, http://www.remss.com). RSS provides daily 3 day-averaged gridded SST at a $1/4^\circ$ resolution for latitudes lower than 38° (http://www.ssmi.com/sst/microwave_oi_sst_data_description.html). An important feature of the microwave retrievals is that they are insensitive to atmospheric water vapor and thus can measure SST through clouds [*Wentz et al*., 2000]. This is a relevant issue over oceanic eastern boundary regions characterized by extended low-cloud coverage, such as the Humboldt upwelling system. We use the daily Optimally Interpolated (TMI-OI) SST product [*Reynolds and Smith*, 1994]. In this data set, the aliasing by the diurnal cycle due to the sun-asynchronous orbit of TRMM satellite is corrected by a simple empirical model of diurnal warming [*Gentemann*, 2003] and an extensive land-mask is applied to remove land contamination [*Gentemann et al*., 2010]. Although this limits the analysis of near-coastal regions, in particular those dominated by coastal upwelling dynamics, it has been shown that TMI-OI data allow identifying the signature of upwelling variability at subseasonal scale further offshore (cf. *Goubanova et al*. [2013] for the Central Benguela upwelling system).

2.2. Global Reanalysis

2.2.1. Atmospheric Reanalysis

The outputs of the European Center for Medium Range Weather (ECMWF) ERA-Interim reanalysis [*Uppala et al*., 2005] are used as surface heat and water forcings for our ocean simulations (see section 3.1). We used daily averages of surface fields (specific humidity, 2 m air temperature, 10 m wind speed, shortwave, longwave heat fluxes, and precipitations) at the model resolution, i.e., on a T255 horizontal resolution. ERA-Interim product improves upon the ERA-40 reanalysis used in *Schweiger et al*. [2008], offering enhanced resolution with 60 vertical levels, improved model physics, and radiative transfer model. The data set spans 1979 to present (continuing in real time), however this study concentrates on the time period from January 2000 to December 2008. This product is considered as our best option for forcing the regional model in terms of heat fluxes since it shows improvements over the NCEP reanalysis [*Bromwich et al*., 2006].

2.2.2. Oceanic Reanalysis

Outputs of the Simple Ocean Data Assimilation (SODA) model are used for determining the characteristics of the long equatorial waves during the 2000–2008 period and are also prescribed as initial and lateral

boundary conditions for our regional model simulations. The SODA reanalysis project, which began in the mid-1990s, is an ongoing effort to reconstruct historical ocean climate variability on space and time scales similar to those captured by the atmospheric reanalysis projects. SODA 2.1.6 uses a general circulation ocean model based on the Parallel Ocean Program numerics [*Smith et al*., 1992], with an average horizontal resolution of $0.25^\circ \times 0.4^\circ$ and 40 vertical levels, which have 10 m vertical resolution near the surface. Assimilated data include temperature and salinity profiles from the World Ocean Atlas-01 (Mechanical Bathythermograph (MBT), Expendable Bathythermograph (XBT), Conductivity-Temperature-Depth (CTD), and station data), as well as additional hydrography, SST, and altimeter sea level. The model was forced by daily surface winds provided by the ECMWF Forecasts ERA40 reanalysis from January 1958 to December 2001 and then by QuikSCAT wind stress data. The reader is invited to refer to *Carton et al*. [2000] and *Carton and Giese* [2008] for a detailed description of the SODA system.

2.3. Data Filtering

Data and model monthly climatologies are estimated over the 2000–2008 period. Afterward, they are extrapolated onto a daily time axis using cubic splines.

Subseasonal anomalies are the departure from the monthly mean data. A 1–2-1 filter is previously applied to the monthly averaged data which are then extrapolated onto the original temporal resolution (daily or weekly) using cubic spline. In order to ensure that no seasonal cycle remains, the monthly seasonal cycle over the period 2000–2008 is also removed. The transfer function (estimated by computing subseasonal anomalies of a daily Gaussian white noise) characterized by its frequencies at $-1/-3/-10$ dB attenuation (i.e., 79/50/10% of the input power survives) is 117/168/416 day^{-1}.

In order to isolate the variability within the intraseasonal time scales, a band-pass 40–90 days Lanczos filter [*Duchon*, 1979] is applied to the subseasonal anomalies. The total filter length is 121 days.

2.4. EOF Analysis

In order to extract the dominant mode of variability of the subseasonal variability along the Peruvian coasts, we apply a classical Empirical Orthogonal Function (EOF) decomposition [*Toumazou and Cretaux*, 2001] to the data set over the 2000–2008 period in the central Peru region (17°S–7°S) within 5° wide band off the coast. We choose to normalize the spatial patterns (hereafter referred to as EOFs) and the associated time series (namely, Principal Components or PCs) such as the standard deviation of the time series is equal to one.

2.5. Wavelet Analysis

Wavelet analysis is used to detect time-frequency variations within time series data. A detailed description of the wavelet analysis can be found in *Torrence and Compo* [1998]. In this study, in order to document the time frequency characteristics of the subseasonal fluctuations, we use the Normalized Wavelet Power Spectrum (NWPS) described in *Goubanova et al*. [2013], based on the Morlet function ($\omega_0 = 6$). It allows for comparing the magnitude of the wavelet spectrum at different frequencies. In particular, the time average of NWPS (or Global NWPS) is composed of local variance contributions to the total energy of the time series and remains independent of the wavelet spectrum scale resolution. We will estimate global NWPS, i.e., time-averaged NWPS, and also perform monthly climatology of NWPS.

Following *Torrence and Compo* [1998], significance levels are determined from $\chi 2$ distribution (with a number of degree of freedom ν) using a background spectrum defined as a first-order autoregressive process having the same variance and autocorrelation at lag -1 as our data. For a time-averaged NWPS, ν depends on the number of points to average (n_a) and can be estimated from *Torrence and Compo* [1998, equation (23)]. In the case of the global NWPS, n_a corresponds to the total number of days within the considered period, whereas for the 8 year monthly climatological spectrum, we take n_a equal 240 (8 years $\times$ 30 days per month).

3. Regional Ocean Model Configuration

Our approach is based on the experimentation with a regional oceanic model of the Peru-Chile region, validated from satellite and in situ observations. Overall, the model is skillful in simulating most aspects of the mean state and variability, comparable to former studies using the same model but within different

configurations (domain, resolution, and boundary forcings). The reader is invited to refer to Appendix A for the detail of the validation.

3.1. ROMS Ocean Model Configuration

Oceanic simulations were performed with the AGRIF version [*Penven et al*., 2006; *Debreu et al*., 2012] of the Regional Ocean Modeling System (ROMS [*Shchepetkin and Mc Williams*, 2005]) version 2.1. ROMS is a split explicit, free-surface, topography-following coordinate model that solves the primitive equations based on the Boussinesq and hydrostatic approximations. Subgrid-scale vertical mixing is parameterized using a K-Profile Parameterization (KPP) boundary layer scheme [*Large et al*., 1994]. The topography is derived from the GEBCO_08 global elevation database at 30 arc-second spatial resolution (http://www.gebco.net).

The ROMS model is used here at an eddy-resolving resolution (1/6° at the equator) in the region extending from 40°S to 15°N, and from the coast to 100°W with 32 sigma-coordinate vertical levels stretched within the surface layer. This configuration is the same than the one used in previous recent studies [*Echevin et al*., 2012; *Belmadani et al*., 2012; *Cambon et al*., 2013; *Brochier et al*., 2013]. The horizontal grid resolution of 1/6° (≈18 km) was selected here as a trade-off between the need to resolve coastal upwelling processes and the computational costs associated with the numerous sensitivity experiments. Although mesoscale eddies are well resolved at 1/6° resolution, especially off Peru (since the wavelength associated with the first baroclinic Rossby radius along the coast of the region of interest varies from ∼600 km near the equator to ∼200 km at 35°S), at such resolution the frictional boundary layer along the slope is not. *Marchesiello and Estrade* [2010] showed in particular that for the Peru coast, the scale of the upwelling is only ∼5 km, which can only be resolved reasonably with a resolution of at least ∼2 km. Here, like in most of the regional modeling studies of this region that use a lower resolution [*Penven et al*., 2005; *Montes et al*., 2010], we will assume that upwelling dynamics is still well accounted for by our model setup.

At the three lateral open boundaries, mixed active-passive conditions are used [*Marchesiello et al*., 2001] with forcing data from the SODA reanalysis 2.1.6. For momentum and tracers, a third-order upstream biased advection scheme is used [*Shchepetkin and McWilliams*, 1998]. Explicit lateral viscosity is null everywhere in the model, except in sponge layers near the open boundaries where it increases smoothly on several grid. Note also that, at lateral open boundaries, a linear adjustment of the model bathymetry to the SODA bathymetry is made within a 2° band. A bulk formulation [*Kondo*, 1975] is used to compute surface turbulent heat, based on ERA-Interim Reanalysis daily mean atmospheric fields (2 m air temperature, relative humidity, surface wind speed, net shortwave and downwelling longwave fluxes, and precipitations), while the wind stress forcing comes from the daily QuikSCAT data. Note that, in order to fill in the QuikSCAT blind zone, an extrapolation of the QuikSCAT momentum fluxes was performed using a simple near-neighbor procedure. For the initialization, SODA potential temperature, salinity, and horizontal current fields were used.

To diagnose the processes responsible for the surface temperature variability associated with the intraseasonal regime, the heat budget within the time varying mixed layer is computed online. The mixed-layer depth (h) is determined by the KPP vertical mixing scheme. The reader is invited to refer to *Menkes et al*. [2006] for more details on such heat budget computations.

Hence, the rate of change of the mixed-layer temperature is driven by the advection terms (**X-ADV**, **Y-ADV**, **Z-ADV**), the mixing terms (vertical diffusivity at the mixed-layer base (**DIFF**) and entrainment/detrainment term (**ENTR**)) and the heat flux term (**FORC**), such as:

$$\partial_t\langle T\rangle = \underbrace{-\langle u\partial_x T\rangle}_{\mathbf{X-ADV}} \underbrace{-\langle v\partial_y T\rangle}_{\mathbf{Y-ADV}} \underbrace{-\langle w\partial_z T\rangle}_{\mathbf{Z-ADV}}$$
$$\underbrace{-\frac{1}{h}(k_z\partial_z T)_{z=-h}}_{\mathbf{DIFF}} \underbrace{-\frac{1}{h}\partial_t h\times(\langle T\rangle - T_{z=-h})}_{\mathbf{ENTR}} + \underbrace{\frac{Q*+Q_s-Q_P}{\rho C_P h}}_{\mathbf{FORC}}$$

where T is the model potential temperature; (u, v, w) are the components of ocean currents; k_z is the vertical diffusion coefficient; Q_S the net surface solar heat flux, and Q_P is the fraction of solar radiation that penetrate below the base of the mixed-layer depth (h). Q* contains the sum of the other surface heat flux terms,

Table 1. Description of ROMS Experiments: Name, Open lateral Boundary Conditions (OBC), QuikSCAT Wind Stress Specifications, and Prescribed Fields for Heat/Water Flux Bulk Formulation

EXP-Name	SODA OBC (E)	QS Wind Stress (W)	HF Bulk Fields (Q)
$ROMS^{CR}$	Total	Total	Total
$ROMS^{E}$	Total	Climatology	Climatology
$ROMS^{WQ}$	Climatology	Total	Total
$ROMS^{W}$	Climatology	Total	Climatology
$ROMS^{CLIM}$	Climatology	Climatology	Climatology

i.e., longwave radiations, latent and sensible heat fluxes. Brackets denote the vertical average over the mixed-layer depth: $\langle T \rangle = \frac{1}{h}\int_{-h}^{0} T dz$.

The simulations were performed over the 2000–2008 period, during which daily averages of all tendency terms, as well as model state variables (temperature, currents, and sea surface height) were stored. The model solution reached a statistical equilibrium (in terms of upper ocean stratification and eddy kinetic energy levels) after 3 year of spin-up performed by repeating the year 2000.

Our confidence in the model configuration results in its realism as evidenced by the detailed validation of the model control run experiment (hereafter referred to as $ROMS^{CR}$) which indicates that it is skillful in simulating most aspects of the mean state and variability (see Appendix A). This model configuration provides a benchmark for evaluating sensitivity experiments to surface forcing and open boundary conditions.

3.2. Experiments Descriptions

We carried out a set of five experiments in order to assess the oceanic response to wind stress, heat fluxes and long equatorial waves at subseasonal time scales in the coastal central region of Peru and thereby interpret the observations. All the experiments only differ by their boundary conditions (either climatological or "real time"). Their setups are summarized in Table 1.

First, the control run experiment ($ROMS^{CR}$) is performed using the 5 day-mean SODA Ocean Boundary Conditions (OBC), the daily QuikSCAT wind stress forcing and with daily bulk formulation input fields for heat fluxes estimations, as described in subsection 3.1. Then, in order to isolate the impact of the distant long equatorial wave signal transmitted as coastal trapped waves along the coast of South-America from the local subseasonal atmospheric forcings, the simulation $ROMS^{E}$ uses the 5 day-mean SODA OBC along with prescribed climatologic atmospheric conditions (wind stress and inputs for bulk formulae). The experiment that has no remote subseasonal equatorial forcing (climatological OBC), while subseasonal local atmospheric forcing is included in the surface boundary conditions is called $ROMS^{WQ}$. Under the hypothesis of linearity, these model experiments can be used to infer the respective role of the IEKW and local forcing on the SST variability along the coast of central Peru.

A complementary experiment was carried out in which the model is forced by prescribed climatological OBC and surface heat flux (for bulk formulae), while real-time QuikSCAT wind stress forcing is used. This experiment, $ROMS^{W}$, when compared to $ROMS^{WQ}$ simulation will allow quantifying the respective role of the subseasonal surface heat flux forcing versus the mechanical role of the winds, mixing the surface layer and changing the mixed-layer depth at subseasonal time scale.

At last, in order to quantify the model variability resulting from purely internal dynamics (i.e., nonlinearities), a climatological simulation is performed that used climatologies at boundary conditions (both ocean and atmosphere). This experiment will be referred to as $ROMS^{CLIM}$.

4. Role of the Remote Equatorial Forcing

In this section, as a first step, we document the time frequency characteristics of the IEKW forcing and its seasonal modulation. Then, based on the regional oceanic model experiments, we quantify the forcing mechanisms of the intraseasonal SST along the coast of central Peru.

4.1. Spatiotemporal Characteristics

In order to derive the IEKW amplitude for the most energetic baroclinic modes, we use a methodology similar to the one described in *Dewitte et al.* [2003]. It consists in a modal (both vertical and horizontal)

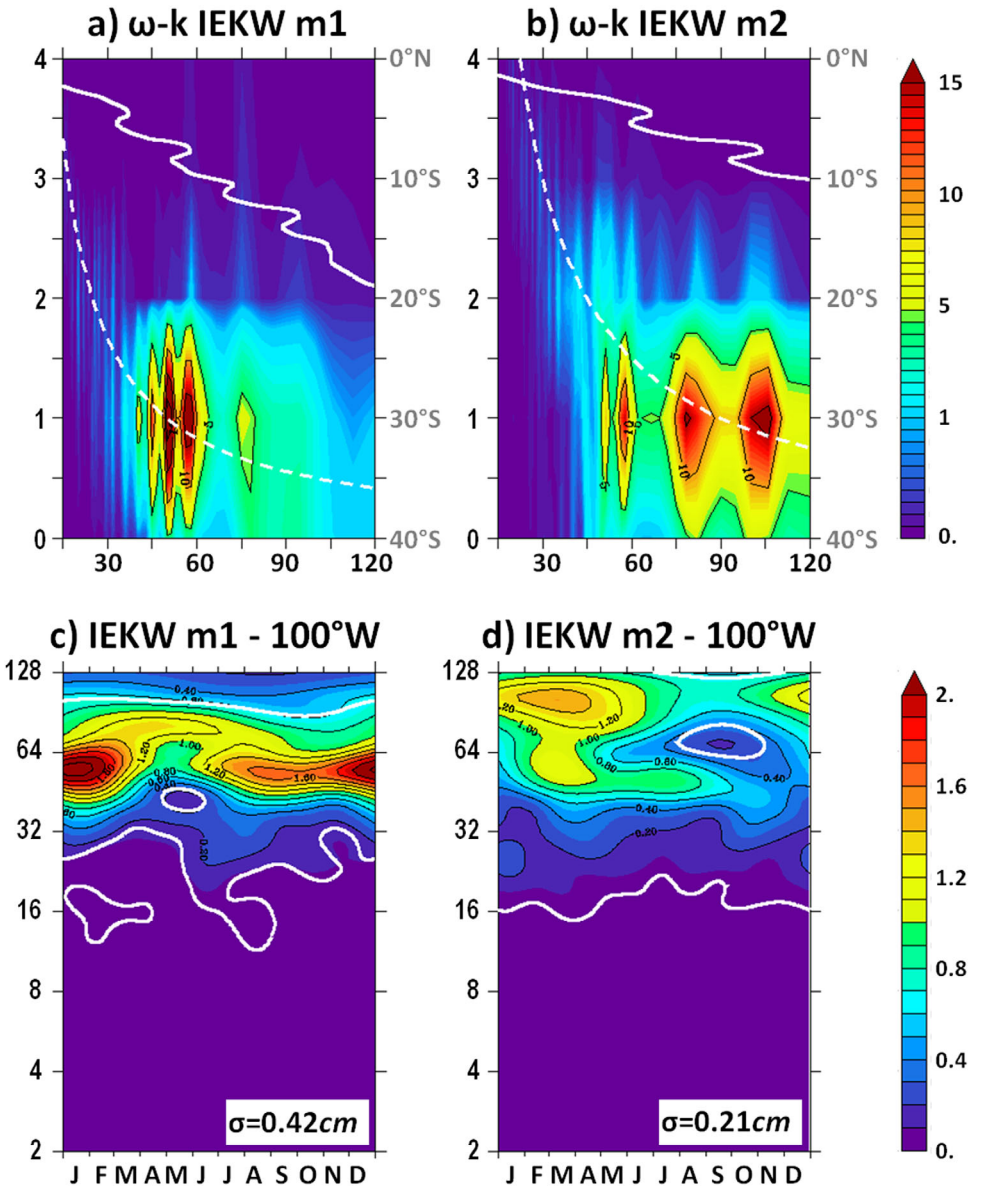

Figure 2. Intraseasonal Equatorial Kelvin Wave (IEKW) Sea Level contribution: (top) Space-time power spectral density [see *Hayashi*, 1982] in the equatorial Pacific for the (a) first and (b) the second baroclinic mode as function of basin split (left scale) and period in days (bottom scale). Units are cm^2. White dashed lines indicate theoretical dispersion curves. White plain lines show theoretical critical latitudes curves (right scale). (bottom) Climatology of the NWPS estimated over the period June 2000 to May 2008 for (c) the first and (d) the second baroclinic modes at 100°W. White line shows the 95% confidence level. For each baroclinic modes, IEKW amplitudes are first normalized by their standard deviation averaged along the equator (140°E–80°W), σ (indicated in the lower right corner).

decomposition of the zonal current and pressure variability. This provides estimates of the Kelvin and Rossby waves contribution to sea level anomalies according to the most energetic baroclinic modes. Applied to the SODA data over the 2000–2008 period, we find, consistently with the results of *Dewitte et al.* [2008a], that the first three baroclinic modes are the most energetic, explaining up to 60% of the total SLA intraseasonal variability (correlation with the total SLA > 0.75). A space-time spectral analysis of the IEKW for the first two baroclinic modes (Figures 2a and 2b) highlights the rich spectrum of energy of long-wavelength ($k \leq 2$) intraseasonal Kelvin wave contributions for the gravest baroclinic mode. This analysis shows the propagation of long-wavelength Kelvin wave since the dominant density peaks fits the theoretical dispersion curve (white dashed lines). The latter is derived from the vertical mode decomposition based on the zonally averaged phase velocity (140°E–80°W). IEKW energy is found between 40−60 days and at

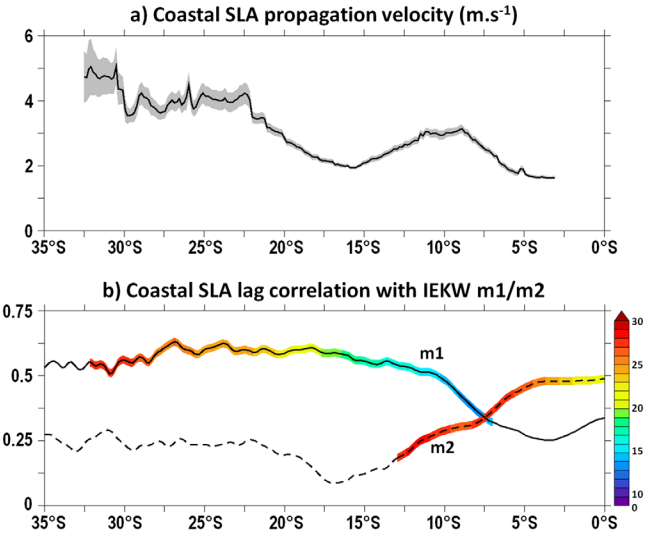

Figure 3. (top) Propagation velocity of the 0.5° coastal band averaged Sea Level intraseasonal Anomalies (SLA). At each latitude, the maximum lagged correlation between the coastal SLA at that latitude and the coastal SLA within a centered 7° latitudinal window is computed. For each 7°-window, the linear regression coefficient that best fit the lag estimation is calculated. Shading indicated error in the linear regression coefficient estimation. Unit is m s^{-1}. (bottom) Maximum lagged correlation between coastal (0.5° coastal band averaged) SLA with the first (second) Intraseasonal Equatorial Kelvin Wave (IEKW) mode at 100°W as a function of latitude in plain (dashed) line. Lag (in days) is specified with color shading. Positive value indicates that equatorial variability leads.

∼75 days for the first baroclinic mode and between 50–60 days and at ∼80 and ∼100 days for the second one. At these frequencies, these waves are trapped along the coast from 5°S as revealed by the values of the theoretical critical latitudes [*Clarke and Shi*, 1991] estimated from the model topography and mean stratification (see plain white line, right scale).

Considering the marked seasonal dependence of the intraseasonal SST variance (Figure 1c), it is interesting to investigate whether the IEKW activity exhibits comparable characteristic. The Figure 2 (bottom) displays the climatology of the Normalized Wavelet Power Spectra (NWPS) of the IEKW at the western boundary of our model configuration (100°W). This analysis reveals that, for the 2000–2008 period, the gravest baroclinic modes experience larger variability during the extended Austral summer season than during the extended Austral winter, which is comparable to the SSTA spectrum. This suggests a priori a likely influence of the IEKW on SST off central Peru.

The following section is devoted to the analysis of the model simulations, which serves as material for the interpretation of the above observations.

4.2. Model Results

In this section, we analyze the outputs of $ROMS^{E}$ experiment (see Table 1), in which the model is forced by climatological surface forcings, and SODA 5 day-mean outputs are prescribed at the three open lateral boundaries. In this configuration, the coastal SST variability off Peru and Chile is predominantly under the influence of the equatorial variability, but it is also driven by the internal model variability (mesoscale activity). Coastal-Trapped Wave (CTW) propagations are expected in the intraseasonal frequency band [*Brink*, 1982; *Belmadani et al.*, 2012], which we observe in $ROMS^{E}$, based on the analysis of SLA averaged within a 0.5° coastal fringe. The values of the mean phase speed associated to the SLA propagation are estimated based on the linear fit of the scattered plot providing the lag that maximizes the lagged correlation between the SLA at a given latitude and the SLA within a centered 7° latitudinal window, as function of the distance (Figure 3a). It indicates that the phase speed ranges from 1.7 to 3 m s^{-1} between 5°S and 25°S, which is consistent with observations [*Spillane et al.*, 1987]. Since coastal SLA is the superposition of the contributions of the various baroclinic modes along the coast, the latitudinal variation in mean phase speed can be interpreted as resulting from the different dissipation rates of the gravest baroclinic modes. In particular, the second baroclinic mode is mostly influential in the northern part but dissipates faster southward than the first mode which thereby dominates the SLA variability. This is illustrated by the lagged-correlation analysis between $ROMS^{E}$ coastal SLA and the IEKW at the western boundary of our model domain (100°W) for the first two baroclinic modes (Figure 3b). It shows that the correlation for the first mode becomes only significant at ∼7°S and reaches 0.5 only at ∼12°S, whereas for the second mode, it gradually decreases to become not significant at 13°S. Note that similar results were obtained when analyzing $ROMS^{CR}$ outputs but with lower correlation values.

The comparison of the model experiments further reveals that the SLA variability within the intraseasonal regimes (40–90 days) can in fact be accounted for by almost the sole equatorial forcing (Figure 4). For instance, the ratio of variance between $ROMS^{E}$ ($ROMS^{WQ}$) and $ROMS^{CR}$ estimated for the 40–90 day^{-1}

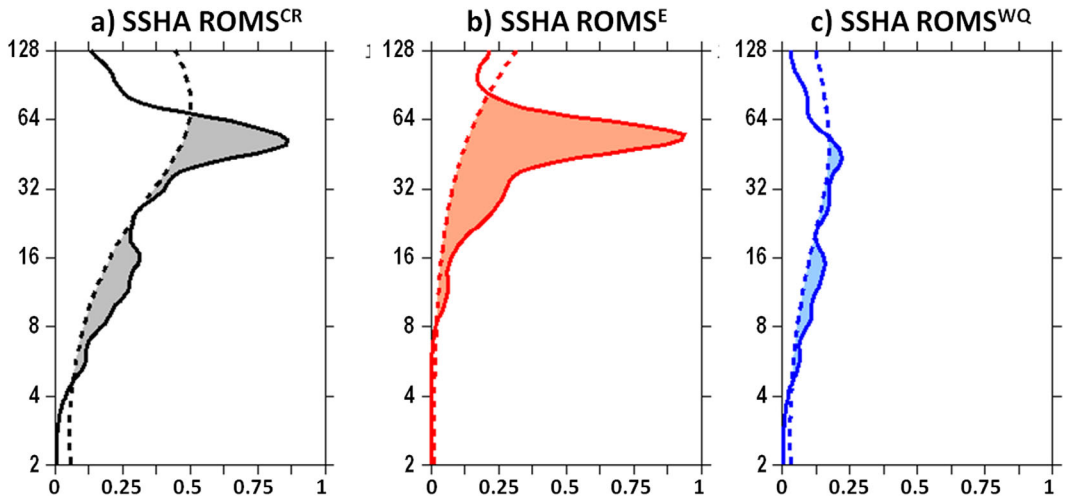

Figure 4. Coastal (0.5° coastal band averaged) SSH averaged between 16°S and 8°S: (top) Global NWPS of subseasonal SSH for (a) $ROMS^{CR}$ simulation, (b) $ROMS^{E}$ simulation, and (c) $ROMS^{WQ}$ simulation. Unit is cm^2. (bottom) Dashed lines indicate the 95% confidence level.

frequency band for Central Peru Coastal SLA averaged between 16°S and 8°S within the 0.5° width coastal fringe (denoted hereafter as CPC time series) is 95% (24%). Note that the internal model variability as inferred from the analysis of the outputs of $ROMS^{CLIM}$ has a weak signature on the CPC-SLA variability (ratio = 7%). These results are not surprising and just validate our modeling framework that is able to simulate the IEKW connection along the coast expected from linear theory.

More interestingly, it is now worth examining how the equatorial variability impacts the intraseasonal SST variability along the coast of central Peru. Figure 5 (top) displays the global NWPS of the SST intraseasonal anomalies averaged in the 0.5° coastal band between 16°S and 8°S (CPC-SSTA) for the same three experiments ($ROMS^{CR}$, $ROMS^{E}$, and $ROMS^{WQ}$). The results indicate that the IEKW is in fact only marginally influential on the SSTA variability along the coast, since within the intraseasonal frequency band 40–90 day^{-1}, only 23% of the energy of the SST variability originates from the connection with the equatorial variability. The climatological NWPS of the CPC-SSTA (not shown) highlights that the peak season of SST variability in $ROMS^{E}$ is in Austral summer, in agreement with $ROMS^{CR}$ and with the IEKW activity. It is worth noting that $ROMS^{CLIM}$ experiment shows that the internal model variability represents 11% of $ROMS^{CR}$ CPC-SSTA variability in the intraseasonal frequency band. In addition, we find that there is little coherency between $ROMS^{E}$ and $ROMS^{CR}$ off central Peru (Figure 5d). For instance, the maximum lag correlation between the $ROMS^{E}$ and $ROMS^{CR}$ CPC-SSTA does not exceed 0.1 over the whole record. Still there are periods when the time series covary, like in February-March 2002 and April-June 2006, indicating that the IEKW can be influential on SSTA episodically along the coast. The spectrum for the simulation using climatological conditions for the open ocean lateral boundaries and daily real-time atmospheric forcing ($ROMS^{WQ}$) confirms that the local atmospheric fluxes are the dominant forcing to explain the SSTA peak in the frequency band 40–90 day^{-1} since the spectrum for $ROMS^{CR}$ and $ROMS^{WQ}$ are comparable (ratio = 93%).

Considering the comparable seasonal variability of the IEKW activity and SST (cf. Figures 2c, 2d and Figure 1c), the model results are counterintuitive and calls for investigating the mixed-layer processes associated with the local atmospheric forcing.

5. Role of the Local Atmospheric Forcing

Dewitte et al. [2011] showed that the wind stress intraseasonal anomalies along the coast of Peru are characterized by a peak variance in Austral winter; especially within the frequency range 2–40 day^{-1}. This is illustrated in Figure 6 that presents the dominant EOF mode of QuikSCAT surface meridional and zonal Wind Stress Anomalies (WSA) that captures 76% of the total variance of subseasonal anomalies. The spatial pattern portrays WSA of the same sign over the entire region with upwelling-favorable south-east (upwelling unfavorable north-west) direction for positive (negative) WSA anomalies (Figure 6a). The maximum

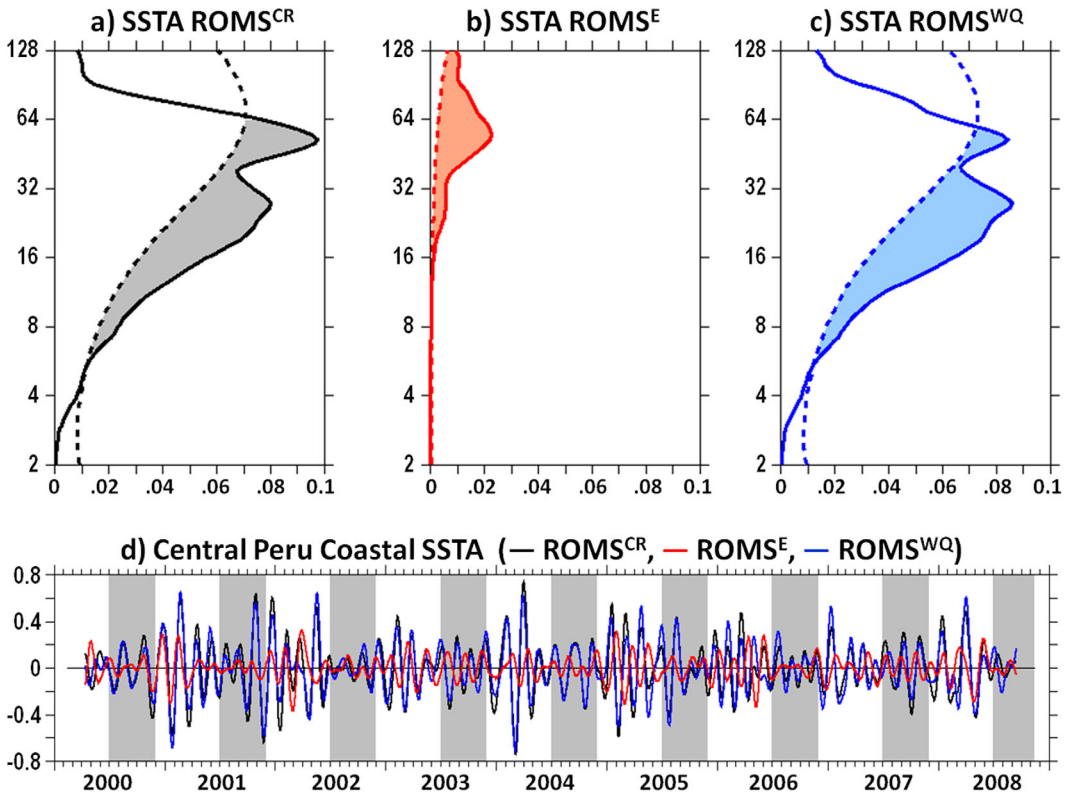

Figure 5. Top plots are the same as Figure 4 but for central Peru coastal SST analysis. Unit is $^{\circ}C^2$. (bottom) Time series of intraseasonal SST (SSTA, 40–90 days) from ROMS^{CR} (black), ROMS^{E} (red), and ROMS^{WQ} (blue) simulations. Gray vertical bands show the July to October season. Unit is $^{\circ}C$.

amplitude of anomalies is found 200 km offshore Pisco. The climatological normalized wavelet power spectrum of the associated time series (Figure 6b) indicates that the largest amount of the wind stress energy is confined in the 2–40 day^{-1} frequency band, during the Austral winter, from June to September. In contrast, the intraseasonal oscillations (40–90 days) represent only 8.7% of the total variance of the PC1 time series, and are hardly significant in July and August, and not significant in Austral summer. These observations question to which extent, such wind forcing can explain the SST peak variance in Austral summer. Further, which mixed-layer processes are associated with such a weak wind?

5.1. Composite Evolution of an Intraseasonal Event

As a first step, we analyze the evolution of a composite intraseasonal event as simulated by the ROMS^{WQ} configuration, for which only the surface forcing undergoes subseasonal variations, while oceanic lateral boundary conditions are prescribed using climatologic conditions (see Table 1). The compositing procedure is based on a previous EOF analysis of the SSTA that is used to trace major intraseasonal events along the dominant mode principal component (time series; Figure 7a). The dominant EOF mode of SSTA in ROMS^{WQ} explains 18% of the subseasonal variability and has a spatial pattern that closely resembles the one of Figure A6a (not shown). The associated time series (PC1-SSTA) has been filtered in order to retain only the intraseasonal time scales using a 40–90 days Lanczos filter. As the local surface forcing is dominant to explain the coastal intraseasonal SST variability off central Peru, this time series compares very well with the one shown in Figure A6d, with a correlation (RMS differences) larger (smaller) than 0.95 (0.16°C). The compositing procedure requires the selection of the strongest intraseasonal events (cold and warm), i.e., that have a local maximum amplitude (in terms of absolute value) larger than 1.25 times the standard deviation. Here it is important to keep in mind that the sign of the PC1-SSTA is defined with respect to the 1st EOF pattern which portrays negative anomalies. This implies that positive (negative) values of the time series are associated with cold (warm) SST events. In this way, we identified 34 events (17 cold events and 17 warm events, cf. blue and red stars in Figure 7a). Note that most of the peaks occur during the extended Austral

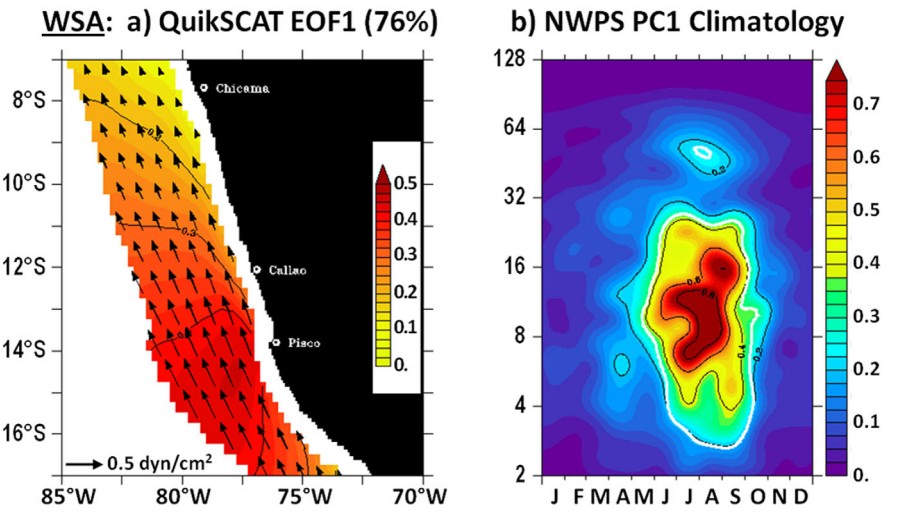

Figure 6. First mode of the bivariate EOF analysis of the subseasonal anomalies of the surface wind stress from QuikSCAT data: (a) Spatial pattern (dyn/cm^2) showing wind stress vectors (arrows) and wind stress magnitude (color shading). (b) A 8 year climatology of the NWPS for the wind stress PC1 (PC1-WSA) estimated over the period June 2000 to May 2008. White line shows the 95% confidence level.

summer season, consistent with the periods of highest SST variability for the intraseasonal regime as identified from the wavelet analysis (Figures 1c and A6c). As the PC1-SSTA time series is not skewed, the composite represents here the average of any variable for all 34 dates identified (i.e., using both cold and warm events). Note that we chose to map the negative phase of the variability, i.e., the processes associated with intraseasonal upwelling events. Therefore, the composite corresponds to the mean of the negative events from which we subtract the mean of the positive ones. The time for this event is denoted as "day 0." Confidence levels are estimated based on a bootstrap method using 10,000 samples and only significant anomalies at the 90% level are displayed on Figures 7 and 8.

The results of the composite analysis of the ROMS^{WQ} outputs are presented in Figure 7 for the mixed-layer temperature (T_{MLD}) and the surface wind stress, and temperature and current anomalies along sections perpendicular to the coast at 11°S at lags −14 days, −7 days, 0 day, and +7 days. This allows us to describe the spatial and temporal evolutions of oceanic conditions and surface wind stress associated with the intraseasonal regime. At a lag of −20 days (not shown), upwelling favorable winds start to blow and positive vertical current anomalies can be detected along the shelf. At a lag of −14 days, winds intensify and weak negative T_{MLD} anomalies (∼0.1°C) can be observed in a narrow coastal fringe. They are associated with a shallower coastal thermocline and a deeper mixed layer (reflecting a change in the vertical stratification). The core of maximum upwelling favorable winds undergoes a southward propagation, with the largest amplitude observed at 16°S for a lag of −7 days. However, at this date, coastal vertical currents have drastically weakened. At this date, the T_{MLD} anomalies have grown and they start to expand offshore, as zonal current anomalies within the mixed layer drive them offshore due to the Ekman divergence. Indeed, T_{MLD} anomalies larger than 0.25°C now occupy a 100 km wide coastal band. In the subsurface, the temperature anomalies can be detected as deep as 250 m, and the coastal thermocline further rises. Note that a second local significant temperature anomaly can be detected ∼350 km off shore, with amplitudes larger than 0.15°C at the surface. The mature phase of the event (lag 0) corresponds to cold temperature anomalies being well developed over the whole region, with maximum amplitude along the coast. They continue their offshore propagation as they are driven offshore by intense zonal current anomalies within the 30 first meters. At this moment, the upwelling favorable winds have drastically weakened, and the anomalous coastal vertical currents turn negative. The following week, the wind anomalies change direction and intensify. This leads to downwelling vertical current anomalies along the shelf and shoreward surface zonal current anomalies within the surface mixed layer. Cold temperature anomalies are still strong but they have weakened at the coast and deepened within the mixed layer. At a lag of +14 days, the temperature returns to near normal conditions (not shown).

Figure 7 thus provides a 3-D description of the evolution of a composite intraseasonal event forced by the winds, which reveals a rather consistent picture with what is expected from Ekman dynamics, although the

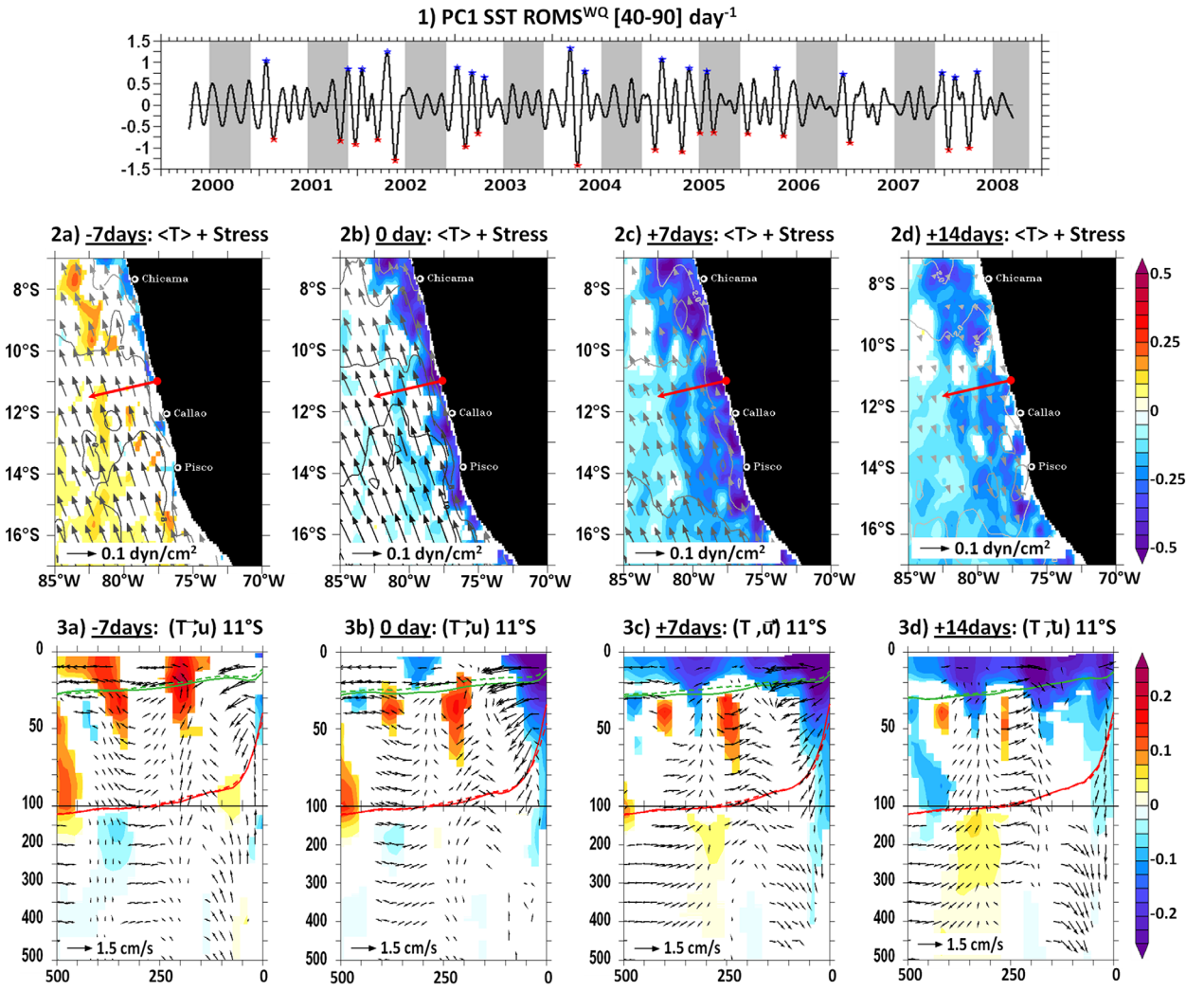

Figure 7. (top) Intraseasonal band-pass filtered PC1-SSTA (40–90 days) for ROMS^{WQ}. Gray vertical bands show the July to October season. (middle and bottom) Time-lagged composites of the intraseasonal anomalies of ROMS^{WQ} outputs for the intraseasonal events identified (see text details). (middle) T_{MLD} (color shading, in °C), wind stress vector (arrows, in dyn/cm^2), and wind stress amplitude (contour, in 10xdyn/cm^2). (bottom) Vertical sections perpendicular to the coast at 11°S in function of depth and distance from the coast (km) of temperature (shading, in °C), cross-shore and vertical currents (arrows, in cm/s). For visualization purposes, mean vertical current amplitude is multiplied by 2000. The plain red (green) line indicates the position of the thermocline for the cold-event composite (mixed-layer depth). The dashed red (green) line indicates the mean position of the thermocline as the average between warm-event and cold-event composite (mixed-layer depth). Fields are represented only when significant at 90% confidence level. The time lags are shown at −14, −7, 0, +7 days.

phase-lag between peak SST and wind stress anomalies is smaller (∼8 days) than a quarter of a period of a cycle, suggestive of the contribution of other processes than just Ekman-induced advection to the rate of SST changes. The latter is devoted to a comprehensive analysis of the processes associated with the SST fluctuations during the composite event of Figure 7.

5.2. Composite Heat-Budget

The contributions of the different processes to the rate of change of the mixed-layer temperature (see details in section 3.1) were computed online to ensure a perfect closure of the budget. In order to smooth the internal model variability and provide an overview of the time sequence of the main processes at work, we derive intraseasonal anomalies from latitudinal averages (16°S–8°S) as a function of the distance from the coast. Figure 8 displays the evolution of the various terms of the heat budget for the intraseasonal regime (bottom, Figures 8f–8l), along with the intraseasonal anomalies of the T_{MLD} (Figure 8a), the mixed-layer depth (Figure 8b), the along-shore wind stress amplitude (Figure 8c), the Ekman pumping velocity (Figure 8d), and the net surface heat fluxes (Figure 8e). In order to ease the interpretation of the time

sequence, visual marks as horizontal lines have been drawn as a guide: Black horizontal lines indicate the mature phase of the event at a lag of 0 day, i.e., when the rate of change of T_{MLD} is zero. The maximum of the upwelling favorable winds are observed 8 days before with values larger than 0.8 dyn cm^{-2} and is highlighted using green dashed horizontal lines. Green dashed lines indicate the minimum in alongshore wind stress at a lag of −22 days and the maximum of the downwelling favorable wind stress 33 days before the mature phase of the event.

Figure 8f shows that the region of maximum cooling rate is located near shore 16 days before the mature phase of the event with a heat loss larger than 4.10^{-2} °C · day^{-1}. A secondary maximum in the cooling rate is detected 350 km offshore at a lag of −11 days with absolute values larger than 2.10^{-2} °C · day^{-1}. Similar patterns are observed for the warming phase between a lag of 0 and a lag of +15 days. The T_{MLD} tendency (**RATE**, Figure 8f) near the coasts portrays an offshore propagating pattern with velocities estimated at ∼0.25 m s^{-1}.

As a first step, we concentrate on the advection terms that result in a straightforward manner from Ekman dynamics (Figures 8g–8i). During the cooling phase (between a lag of −20 days and a lag of 0 day), both vertical (**Z-ADV**, Figure 8i) and zonal advection (**X-ADV**, Figure 8g) are in phase with the **RATE** of change of T_{MLD}, explaining a large amount of its variability. Indeed, the variance explained by the summed-up contribution of **Z-ADV** and **X-ADV** is 63% of the T_{MLD} tendency over a whole cycle for the average within the first 100 km off the coast. Meridional advection (**Y-ADV**, Figure 8h) opposes vertical advection (i.e., a warming tendency) near the coast due to the divergent flow at the surface associated with the upwelling, but this effect remains rather weak. Zonal advection is partly responsible for the offshore propagation of T_{MLD} anomalies. Vertical advection presents two local maxima, one located at the coast which corresponds to the coastal upwelling associated with increased equatorward wind stress, and a secondary maximum located ∼60 km offshore induced by the rather broad pattern of Ekman pumping (Figure 8d). As mentioned earlier, it is interesting to note the 8 day lag between vertical advection and wind stress anomalies that is larger than what is expected from Ekman dynamics.

We can interpret the deviation from Ekman theory in the light of the heat budget that provides estimates of mixing processes. During the developing phase of the event (between a lag of −40 and −15 days) near the coast, the vertical diffusivity at the base of the mixed layer (**DIFF**, Figure 8j) is a cooling term that can be interpreted as resulting from restratification processes [*Fox-Kemper and Ferrari*, 2008] associated with the anomalous conditions of the previous phase. Indeed, the vertical diffusivity term is in quadrature with the rate of change of T_{MLD}, with a coastal cooling rate larger than 4.5 10^{-2} °C · day^{-1} at a lag of −25 days. The entrainment term (**ENTR**, Figure 8k) contributes only slightly to the cooling near the coast but becomes one of the main contributors to the cooling tendency in the off-shore region relative to the other terms. **ENTR** is however smaller than the heat-flux forcing term (**FORC**, Figure 8l) that has a significant contribution to **RATE**. The surface heat-flux forcing can be interpreted as follows (see Figure S1, in Supporting Information): the wind intensification during the developing phase of the event leads to a significant increase of heat loss through surface latent heat fluxes (>8 W m^{-2}). In the first 50 km, small positive anomalies of latent heat fluxes have to be attributed to the colder than normal SST and the weaker mean winds. Here the shortwave heat fluxes are enhanced (∼+1.5 W m^{-2}), while 200 km offshore, the downward longwave heat fluxes are reduced (∼−1 W/m^{-2}). In conclusion, the net surface heat flux is in phase with the wind forcing components and results in an offshore heat loss attributed to evaporation and a small heat gain at the coast. Nevertheless, the heat flux forcing term (**FORC**, Figure 8l) is not directly comparable to the surface net heat flux anomaly because the latter is distributed within the mixed layer that varies during the evolution of an event. To a lesser extent, **FORC** also integrates the residual of the solar flux penetration into the mixed layer, which specifically depends on the mixed-layer depth anomalies. In particular, the wind intensification tends to deepen the mixed layer through vertical mixing. Indeed, 2 days after the maximum wind intensification (reduction), the MLD is 2 m deeper (shallower) than normal over the whole longitudinal extension (Figure 8b). These variations are negligible offshore where the MLD remains relatively deep (MLD >30 m, see Figure 7), but are crucial at the coast, where the MLD rises to a depth of 10 m in Austral summer (see Figures A1c and A3c in Appendix A). Consequently, the surface forcing term, **FORC**, is in phase with the temporal evolution of the MLD (2 days after the wind variability) and exhibits a variability that is more important at the coast, with absolute values larger than 5.10^{-2} °C · day^{-1}.

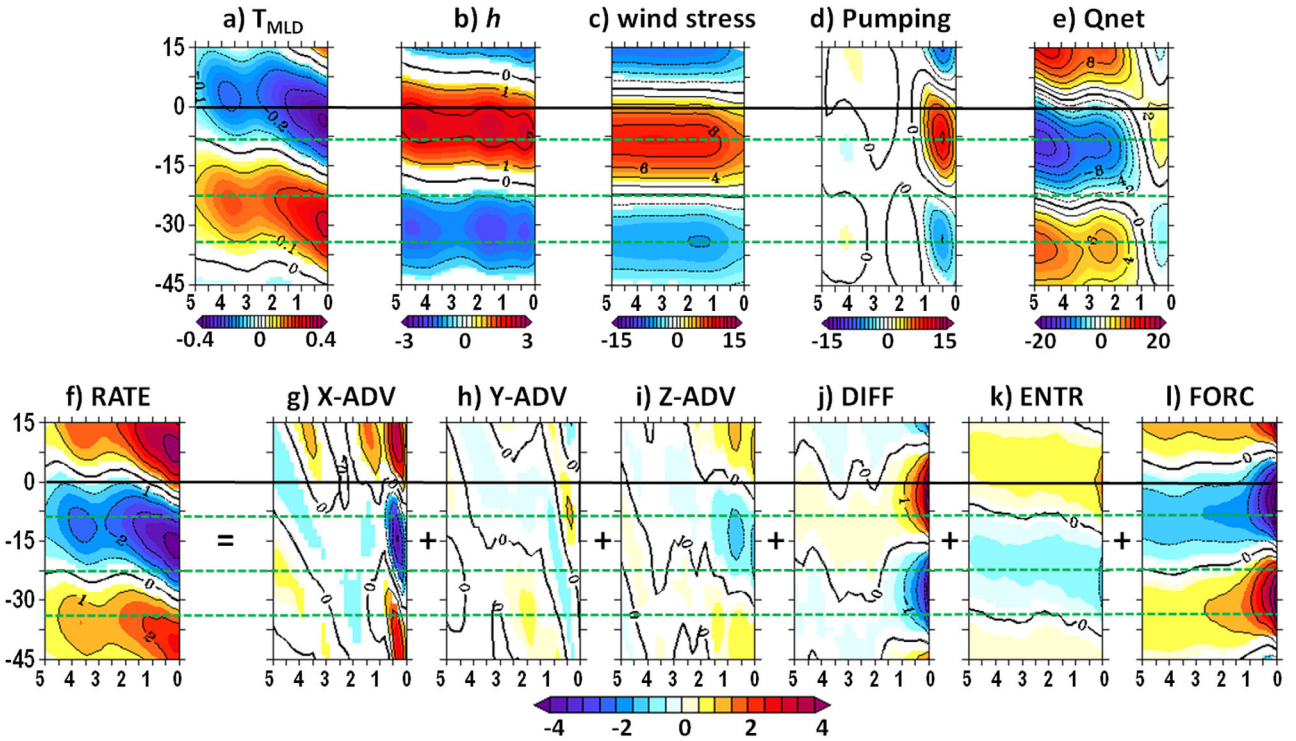

Figure 8. Time-lagged composites of the intraseasonal anomalies of $ROMS^{WQ}$ simulation averaged between 16°S and 8°S as a function of the distance from the coast (in 10^2 km) for the intraseasonal cold events identified based on the 40–90 days band-pass filtered PC1-SSTA from $ROMS^{WQ}$ simulation. (top) The temperature within the mixed layer ((a) T_{MLD}, in °C), the mixed-layer depth ((b) *h*, in m), the along-shore wind stress ((c) 100xdyn/cm^2), the Ekman pumping velocity ((d) positive upward, unit is 10^{-7} m s^{-1}), and the surface net-heat fluxes ((e) Qnet, W/m^2). (bottom) Heat budget results: (f) rate of change, (g) zonal advection, (h) meridional advection, (i) vertical advection, (j) diffusivity at the base of the mixed layer, (k) entrainment, and (l) forcing contribution. Unit is 100x °C · day^{-1}. Color shading indicates significant composites (90% confidence level).

Thus, during the developing phase of the event, mixing and surface forcing are dominant processes, but they tend to compensate each other near the coast. The summed-up contribution of the mixing terms (**DIFF** + **ENTR**, warming) and the surface forcing term (**FORC**, cooling) results in a overall cooling trend in phase with the T_{MLD} tendency with values peaking at $2.2 10^{-2}$ °C · day^{-1} at a lag of −16 days at the coast (not shown). The variance explained by **DIFF** + **ENTR** + **FORC** is 33% of the T_{MLD} tendency over a whole cycle for the average within the first 100 km off the coast, the remaining variance being explained by the advection terms. This compensation effect is allowed by the shallow mixed layer in Austral summer that therefore experiences large variations relative to its mean depth and at the same time favors diabatic cooling that opposes to the enhanced mixing. The shallow mixed layer is also favorable to the enhancement of the influence of Ekman dynamics on SST through anomalous vertical advection of mean vertical temperature [*Goubanova et al.*, 2013].

In order to evaluate the respective role of the surface heat flux forcing versus the mechanical role of the wind, the heat budget was estimated from the $ROMS^{W}$ experiment which considers climatological heat flux forcing. The results (cf. Figure S2 in Supporting Information) show that the off-shore variability (between 300 and 400 km offshore) is drastically reduced in $ROMS^{WQ}$ compared to $ROMS^{W}$. Indeed, the ratio of variances of the rate of SST change between $ROMS^{W}$ and $ROMS^{WQ}$ for the composite intraseasonal anomalies is lower than 30%, revealing that heat flux term is the dominant forcing that triggers offshore SST anomalies. Near the coast, the balance between the tendency terms of $ROMS^{W}$ is qualitatively comparable to $ROMS^{WQ}$ (cf. Figure 8) although with a weaker amplitude due to smaller variations in the MLD. Indeed, the ratio of variances of the T_{MLD} tendency between $ROMS^{W}$ and $ROMS^{WQ}$ and within the first 100 km coastal fringe is larger than 83%. The results of $ROMS^{W}$ thus confirm that the net-heat flux forcing is important in reinforcing SST anomalies through its coupling with vertical mixing variability.

In order to contrast the above results with what happens during the Austral winter when the mixed-layer depth is deeper (see Figure A3c), the similar composite analysis of the tendency terms is performed, but

using the time series associated with the dominant EOF of zonal and meridional wind stress anomalies. The 28 events can be selected that mostly take place during the extended winter season, consistently with the periods of highest WSA variability within the intraseasonal regime (Figure 6b). The heat budget composite reveals that surface heat flux anomalies have a similar amplitude to Austral summer events (cf. Figure S3, in Supporting Information) despite the WSA amplitude being twice as large (cf. Figure 8c). However, the resulting heat flux forcing term is much weaker due to the relative deep mixed layer in Austral winter (Figure A3c from Appendix A). Mixing has also almost no contribution to the rate of SST change. SST intraseasonal variability in Austral winter thus results from Ekman dynamics where zonal and vertical advection terms are the main contributors to the SST changes. These terms remain weak however relative to the intensity of the along-shore wind stress anomalies because of the significantly reduced surface stratification in Austral winter compared to the Austral summer (cf. Figure A3c). In particular, vertical advection is reduced due to the diminished Surface Vertical Temperature Gradient (SVTG) that acts as an efficiency coefficient of the impact of Ekman-driven vertical currents on SST through vertical advection [see *Goubanova et al*., 2013].

6. Discussion and Conclusions

In this paper, we have investigated the forcing mechanisms of the Sea Surface Temperature variability along the coast of Peru based on the experimentation with a regional ocean model that has been previously thoroughly validated with in situ and satellite observations. Our main focus was on the intraseasonal SST regime (40–90 days) described in *Dewitte et al*. [2011] because of difficulties to diagnose its forcing mechanism from just satellite data and the observation that wind stress anomalies are particularly weak within this frequency band, suggesting a privileged role of the intraseasonal equatorial Kelvin wave in forcing this regime. An approach based on sensitivity experiments with a regional ocean model to boundary forcings is adopted. The model experiments, that only differ from either their open lateral ocean boundary conditions and/or the local atmospheric forcings (i.e., climatological or not), reveal that the intraseasonal SST regime is in fact mostly wind driven. This is counterintuitive considering that the energy of the intraseasonal wind stress anomalies is the weakest in Austral summer (i.e., not significant, see Figure 6b), while the equatorial Kelvin wave does propagate along the coast as thermocline fluctuations. This suggests that there is a significant difference in the equatorial oceanic teleconnection for thermocline depth and SST along the coast of Peru, at least over the 2000–2008 period. This is summarized in Figure 9 that shows the ratio (percentage) of variance for the intraseasonal regime (40–90 days) between the simulation ROMS^{E}, where only the intraseasonal equatorial Kelvin wave forcing is considered (see Table 1), with respect to the control run simulation (ROMS^{CR}), for SST (in red) and thermocline depth (15°C isotherm depth, in blue). It indicates that the equatorial Kelvin wave forcing account for at most ∼30% of the intraseasonal SST variability along the coast (maximum at ∼7°S), while the thermocline fluctuations of equatorial origin can easily propagate along the coast as far South as 20°S since the variance of thermocline anomalies in ROMS^{E} remains larger than 70% of ROMS^{CR} North of 20°S.

Thus, on the one hand, model sensitivity experiments reveal that intraseasonal SST regime is forced by the local atmospheric forcing. On the other hand, the wind forcing has a weak variance at intraseasonal time scale, in particular in Austral Summer. This emphasizes the fundamental role of the seasonal variations of the surface stratification for controlling the efficiency by which local winds can produce SST changes at intraseasonal time scales along the coast of Peru through vertical advection. Such conceptual advective model, proposed by *Dewitte et al*. [2011] for interpreting the intraseasonal SST variability off Peru, writes as follows: $\frac{dT}{dt} = -\tilde{w}.\frac{\partial \bar{T}}{\partial z}$, where $\bar{T}$ is the mean temperature and $\tilde{w}$ denotes the intraseasonal anomalous vertical velocity. It has been applied by *Goubanova et al*. [2013] for the central Benguela system considering the seasonal evolution of $\frac{\partial \bar{T}}{\partial z}$ to account for climatological changes in surface stratification. They were able to reconcile similar apparent inconsistency between the seasonal evolution of the wind stress and the intraseasonal SST variability. Here we go beyond this conceptual model by performing an explicit heat budget based on the regional model. The results confirm that the magnitude of surface stratification (i.e., the vertical temperature gradient between the surface and the depth of the base of the mixed layer) determines the efficiency by which wind stress anomalies can force SST anomalies along the coast of Peru through advection processes. Thus, the SST intraseasonal regime during the Austral summer is mostly wind-driven despite the very weak wind stress variability (i.e., ∼6 times weaker than in Austral winter). Still, due to the shallow mixed layer during this season, diabatic processes have a significant contribution to the rate of SST change

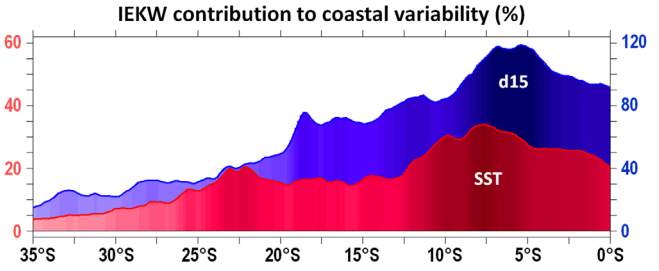

Figure 9. Intraseasonal variability (40-90 days) ratio (%) of variance between ROMS^{E} simulation and ROMS^{CR} as a function of latitude for the SST (red, left scale) and the depth of the 15°C isotherm (d15, blue, right scale) averaged in a 0.5° coastal band.

(∼30%) which is influential on the evolution of SST anomalies. In particular, they favor a faster response of SST to wind stress, reducing the quadrature between SST and wind stress anomalies expected from the conceptual advective model. As a verification test, the simple advective model is applied here to the central Peru region. Vertical velocity anomalies are derived from Ekman transport (i.e., $\tilde{w} = \frac{\tau}{\rho f L_U}$, using an upwelling scale, L_U, ∼25 km) and the Surface Vertical Thermal Gradient is determined either from observations or ROMS^{WQ} (see Figure A3c). The estimated T_{MLD} tendency at the first coastal point exhibits comparable variability than when it is calculated from the output of ROMS^{WQ} (not shown). However, a lag of 8 days between both estimates is observed.

Our results provide material for the interpretation of intraseasonal SST variability off Peru, which may be used for improving forecasting strategies. Current approach for short-term prediction within the ENFEN (Estudio Nacional del Fenómeno El Niño) in Peru consists in monitoring the IEKW activity assuming that it can account for temperature changes along the coast. Our results suggest that at intraseasonal time scale, along-shore winds should be also considered for short-term forecasts of upwelling conditions, which calls for investigating the source of the intraseasonal winds along the coast of Peru. *Dewitte et al*. [2011, Figure 13] showed that they are related to anomalous conditions of the South Pacific anticyclone and suggested that the latter could be related to the Madden-Julian Oscillation (MJO) through atmospheric teleconnections. This issue would deserve further investigation which is beyond the scope of this paper. At this stage, it is interesting to note that a relationship between the MJO and the winds along the coast of Peru would imply that the MJO-induced equatorial Kelvin wave be more elusive along the coast of Peru, which may explain difficulties in inferring anomalous oceanic conditions along the coast of Peru in recent years from just the monitoring of the oceanic equatorial wave (K. Mosquera, personal communication, 2013).

Our results also point out the need to simulate a realistic surface stratification in ocean models for this region since, on the one hand, it determines the efficiency by which SST relates to the winds, potentially acting as a noise amplifier, and, on the other hand, it determines the balance between diabatic and adiabatic processes. This puts a further stringent test to the oceanic regional model in this region as they are being coupled to regional atmospheric models in order to serve as diagnostic tools for understanding the warm biases in the current generation of global coupled models [*Xie et al*., 2007]. Whereas recent concerns have been drawn to the sensitivity of the oceanic circulation to mesoscale features of the along-shore atmospheric circulation (e.g., so-called wind drop-off) [*Capet et al*., 2004; *Renault et al*., 2012], it is likely that coupled ocean-atmosphere regional models may be as sensitive to the mixing parameterizations used in their oceanic component. Our results call for evaluating such sensitivity, which goes along with testing the impact of going toward higher resolution.

At last our study calls for investigating such issue for the coast of Central Chile where an energetic seasonal varying low-level coastal jet is present [*Garreaud and Muñoz*, 2005] having a distinct seasonal evolution than the intraseasonal winds off Peru [*Renault et al*., 2009]. Since intraseasonal Kelvin wave propagation has been observed along the coast of Chile [*Hormazabal et al*., 2002] and that the regional atmospheric circulation is influenced by the MJO [*Julia et al*., 2012], a comparative study would provide interesting material for documenting the range of thermodynamical regimes associated with intraseasonal variability in upwelling systems.

Overall, our study illustrates the complexity of the processes controlling the intraseasonal SST variability along the coast. Attention should thus be paid when using SST for deriving upwelling indexes [*Demarcq and Faure*, 2000], although our findings may not be transposed to all time scales of variability. It also challenges our understanding of the low-frequency variability and long-term trend in upwelling regions which have been interpreted mostly in the light of the Ekman theory [*Bakun*, 1990; *Gutierrez et al*., 2011]. Since mixing appears to contribute to SST changes in the intraseasonal regime, we may speculate that rectification processes could take place

within the mixed layer to explain SST variability at lower frequencies. *Dewitte et al*. [2012], for instance, suggest that the long-term cooling trend off Peru observed in their simulation is related to the rectified effect of the El Niño variability on the upwelling, which implies a nonlinear mixed-layer process at work. Here as a preliminary step, our results call for investigating whether the low-frequency changes in mean state could be influential on the balance of processes explaining the intraseasonal SST regime. In particular, we may wonder if the intraseasonal equatorial Kelvin wave activity that exhibits a low-frequency modulation [*Dewitte et al*., 2008a] may not have been more influential on SST at some other periods of time. As mentioned earlier, this has implications for short-term predictions of regional oceanic conditions off Peru useful for fisheries management, since the IEKW-induced SST would be more predictable than Wind-induced SST anomalies. This is the topic of current research.

Appendix A

In this appendix, we evaluate the control run experiment (referred to as ROMS^{CR}, see Table 1), which consists in running the regional model with the boundary conditions described in section 3.1 (i.e., with the 5 day-mean SODA boundary conditions, the daily QuikSCAT wind stress forcing and with daily bulk formulation input fields for heat fluxes estimations). A special attention is put on the subsurface mean state due to the sensitivity of the mixed-layer processes to the characteristics of the vertical stratification. Therefore, we make use of the available in situ subsurface observations available at IMARPE and from the CARS^{2009} climatology. A careful validation of the model is also required considering that an a priori rather low resolution is used to correctly resolved boundary layer dynamics along the continental slope and therefore the upwelling scale which is of the order of ~5 km in this region [*Marchesiello and Estrade*, 2010]. Such limitation applies to most ocean modeling studies in this region [*Penven et al*., 2005; *Montes et al*., 2010; *Belmadani et al*., 2012] and is not detrimental for achieving a fair realism of most parameters of interest in this study as evidenced from the validation.

A1. In Situ Data

Coastal station SST data, with a monthly resolution, were obtained from five piers of the Peruvian Marine Research Institute (IMARPE) between 4°S and 14°S (Païta at (05°04′45″S–81°06′21″W), Chicama at (07°41′27″S–79°26′16″W), Chimbote at (9°04′22″S–78°36′38″W), Callao at (12°03′00″S–77°09′00″W), and Pisco at (13°48′09″S–76°17′23″W)). For details, the reader is invited to refer to http://www.imarpe.pe/imarpe/index.php?id_seccion=I01080104010000000000.

15°C isotherm depths data: Flores et al. [2010] provide the average depth of the thermocline along the coast of Peru, defined as the 15°C isotherm, over the 1961–2010 period, on a monthly scale. They have compiled temperature data from XBT, CTD, Niskin, and Nansen bottle measurements from historical IMARPE and international cruises. They derived temperature profiles in 2° × 1° bins off the Peruvian coast on a 20 m resolution vertical grid (between 0 and 200 m). This method allows deriving monthly averages with a few gaps, which are filled through linear interpolation [*Flores et al*., 2010]. The 15°C isotherm depth is then derived from the temperature profiles.

CARS^{2009} Temperature Climatology: The 2009 release of the global three-dimensional CSIRO Atlas of Regional Seas (CARS) climatology is used to validate the model mean stratification off central Peru. This climatology combines all the available oceanographic data over the last 50 years, along with Array for Real-Time Geostrophic Oceanography (ARGO) buoy profiles. It is based on rigorous quality controls of input data and an adaptive-length-scale loess mapper to maximize resolution in data-rich regions [*Ridgway et al*., 2002]. CARS^{2009} covers the global oceans south of 20°N on a 0.5° degree grid.

A2. 2000–2008 Mean State

The Figure A1 (top map) illustrates the ROMS^{CR} skill in simulating mean SST, compared to the CARS^{2009} data. Within this configuration, the model simulates a realistic mean SST with spatial correlation between model and observations larger than 0.99 and absolute differences that do not exceed 0.5°C within the coastal central Peru region (on average within a 200 km width coastal fringe from 16°S to 8°S). The Peruvian upwelling signature is clearly marked within a 300 km wide coastal strip between 18°S and 5°S, in agreement with the observations. The mean SST is improved compared to previous nonclimatological studies [*Dewitte et al*., 2012; *Cambon et al*., 2013] because of the use of realistic heat flux forcing combined to the bulk formulation. Differences between model and observations near the coast can be attributed either to

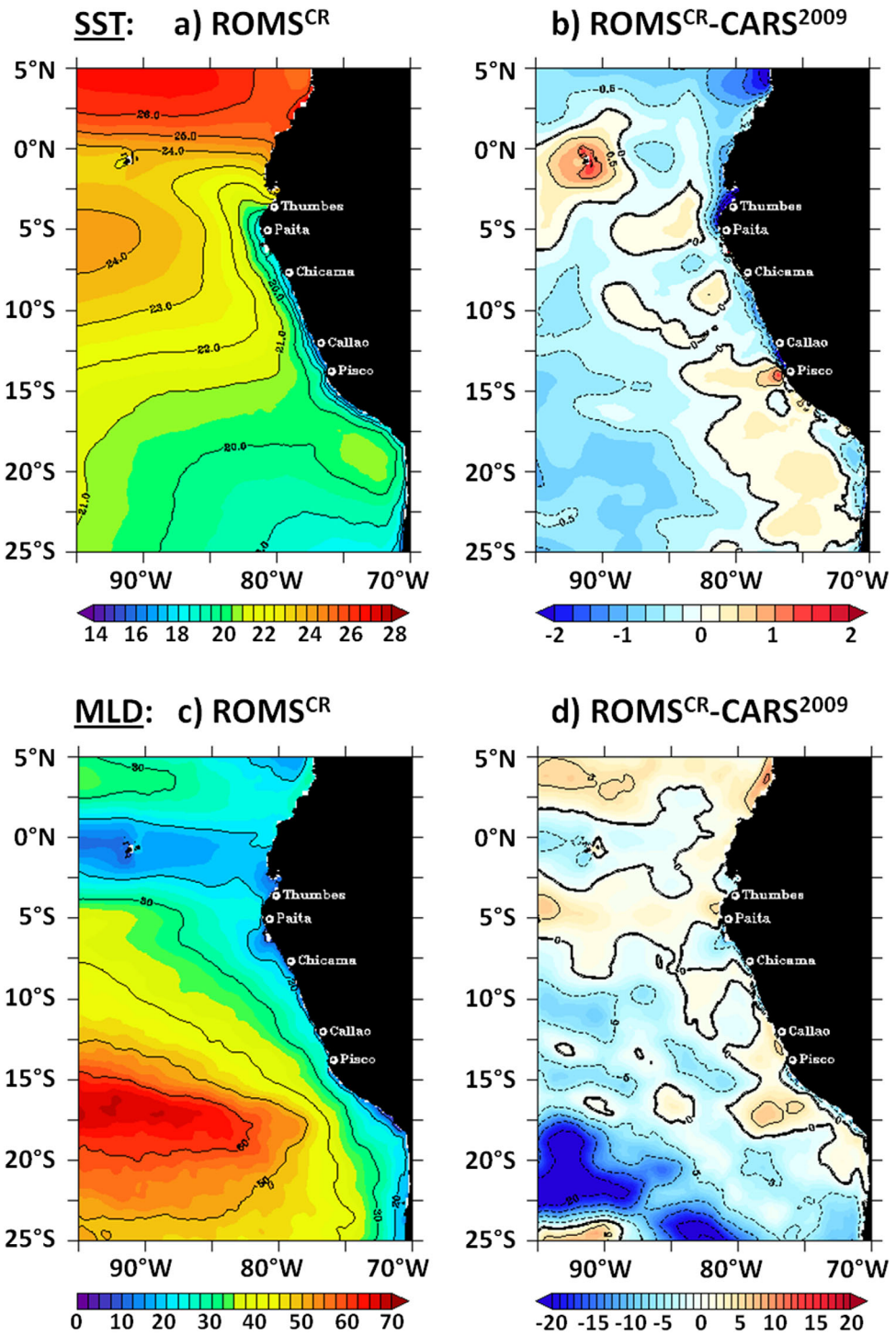

Figure A1. (a) Map of mean Sea Surface Temperature (SST) for the ROMS^{CR} simulation over the 2000–2008 period. (b) Map of the differences between model and observations (CARS^{2009} climatology). Unit is °C. (c) Map of mean Mixed-Layer Depth (MLD) for the ROMS^{CR} simulation over the 2000–2008 period. (d) Map of the differences between model and observations (CARS^{2009} climatology). Unit is m.

warm near-shore bias in the observations [*Dufois et al.*, 2012] or to the overestimation of the wind drop-off near the coast through the extrapolation procedure applied to the QuikSCAT wind product.

In order to evaluate whether the realism of mean SST is reflected in the Mixed-Layer Depth (MLD), Figure A1 (bottom) shows the MLD comparison between model and CARS^{2009} climatology. The latter is defined as

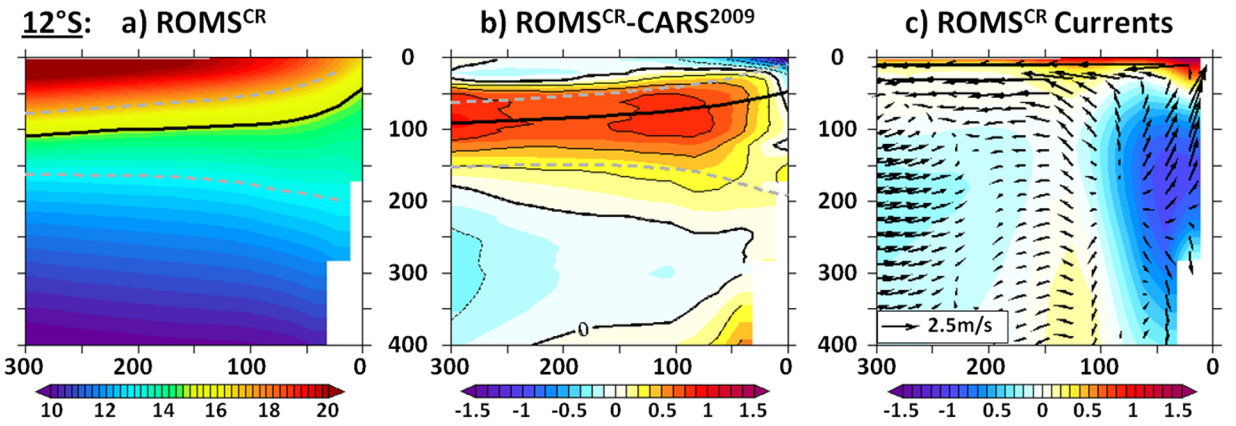

Figure A2. Mean (2000–2008) vertical sections perpendicular to the coast at 12°S in function of depth and distance from the coast (km). (a) Mean temperature for the ROMS^{CR} simulation. The mean position isotherm 15°C (d15) is underlined using black plain lines, and the 13°C (d13) and 17°C (d17) isotherms are depicted with dashed gray lines. (b) Differences between model and observations (contours are drawn every 0.25°C). Observed mean position of d13, d15, and d17 are indicated as in Figure A2a. (c) ROMS^{CR} regional oceanic circulation: mean along shore (color shading, equatorward flows are positive), cross-shore and vertical (arrows) currents. Unit is m s^{-1}. For visualization purposes, mean vertical current amplitude has been multiplied by 2000.

the minimum between an MLD based on a 0.2°C criterion in temperature and an MLD based on a 0.03 criterion in salinity, while ROMS MLD is computed online based on the KPP scheme. ROMS^{CR} agrees well with the observations, with a spatial correlation larger than 0.88. ROMS^{CR} MLD presents a weak mean bias of less than 5 m along the Peruvian coast. Large scale patterns are also qualitatively similar, with deeper MLD over the South and West of the domain. Note that an offline estimation of the ROMS^{CR} MLD, based on the same temperature and salinity criteria as the observations, leads to a slight deeper MLD (by less than 10%): ∼1 m along the coast and ∼6 m in the South-West corner of the domain. This is due to the erosion of the surface stratification through entrainment processes.

To further assess the realism of the simulation in terms of the vertical stratification structure, Figures A2a and A2b compare the ROMS^{CR} simulated cross-shore vertical structure of temperature at 12°S in the upper 400 m with the CARS^{2009} climatology temperature data. ROMS^{CR} mean thermal structure is in rather good agreement with the observations with isotherms tilted upward in the first ∼50–100 km from the coast and within a ∼100 m thick surface layer. In the surface layer (upper 20 m), the simulation is slightly cooler than the observations (∼0.5–1°C, as illustrated in Figure 1b) while at deeper depth near the coast (50–150 m) warmer temperatures are found in the observations. Although this may reflect a model deficiency, it is also likely related to the different periods over which the climatology was calculated. In particular, the period 2000–2008 is characterized by a cooler SST along the coast compared to the period 1976–1999 [*Dewitte et al*., 2012]. Also, in the core of the Peru-Chile Counter Current (PCCC) at 300 km offshore at 230 m depth, the simulation is slightly cooler than the observations (∼0.2°C). Nevertheless, the largest differences are found in the thermocline, where the simulated temperature is on average warmer by 0.5°C. The maximum discrepancies (0.8°C) are found 100 km off shore at 60 m depth. It is associated with a deeper than observed thermocline (∼+15 m, identified as the depth of the 15°C isotherm), with weaker (25%) vertical gradients than in the observations (identified as the thickness of the layer between the 13°C and 17°C isotherms). The rise of the isotherms is associated with a rise of the isopycnals due to the cooler and denser upwelled waters, which creates a cross-shore density gradient driving the surface geostrophic equatorward Peru Coastal Current (PCC), with velocities larger than 1.5 m s^{-1} near the coast. This is illustrated on Figure A2c that displays the cross-shore section of mean circulation at 12°S. The poleward Peru Chile Under-Current (PCUC) is found below the PCC, with its core located over the continental shelf and slope at ∼170 m depth, making it the primary source for the upwelled waters [*Huyer et al*., 1987]. Mean velocities in the core of the PCUC reach ∼12 cm s^{-1}, consistently with previous model studies [*Penven et al*., 2005; *Montes et al*., 2010; *Colas et al*., 2011; *Dewitte et al*., 2012] and with the description given in previous observational studies [*Huyer et al*., 1991; *Strub et al*., 1998]. The PCCC can also be detected at ∼200 m depth 300 km offshore, with poleward velocities ∼0.3 m s^{-1}. A realistic simulation of the alongshore current shear is important since it controls the baroclinic instabilities and the associated eddy activity [*Marchesiello et al*., 2003].

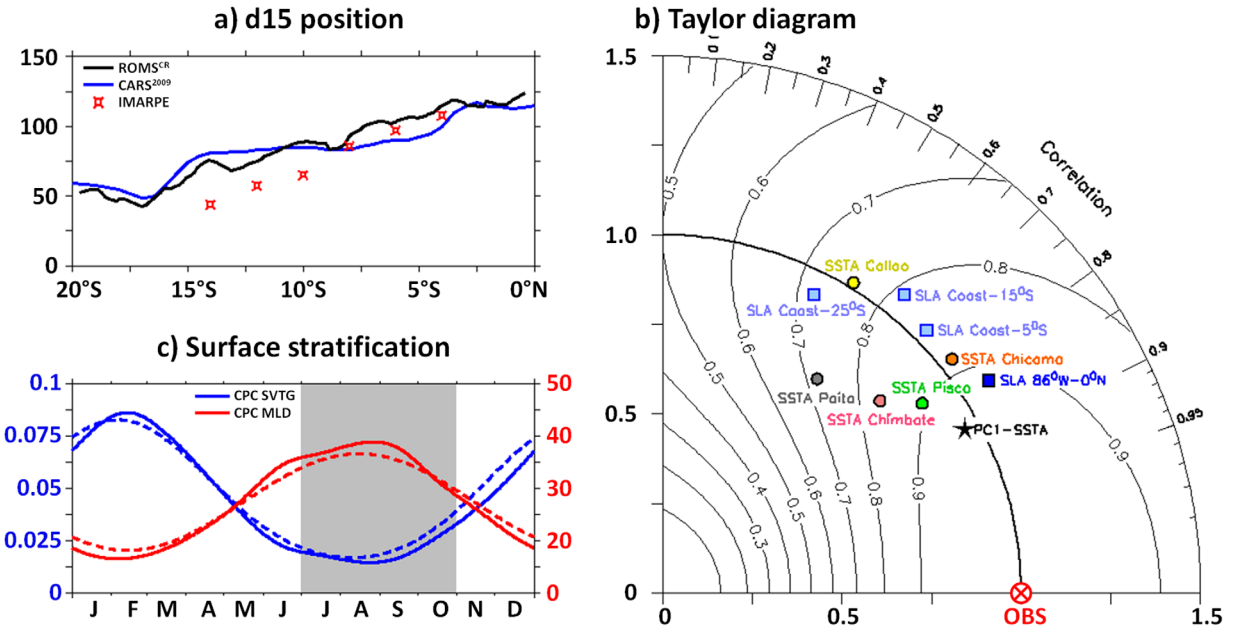

Figure A3. (a) Mean 15°C isotherm depth over the 2000–2008 period averaged within a 1° coastal band as a function of latitude for ROMS^{CR} simulation (black line), IMARPE's climatology (blue line), IMARPE in situ data (red symbols). (b) Taylor diagram illustrating the ROMS^{CR} skills over the 2000–2008 period. The radial coordinate gives the magnitude of total standard deviation, normalized by the observed value, and the angular coordinate gives the correlation with observations. It follows that the distance between the observed point (OBS, red strike-through circle) and any model's point is proportional to the RMS model error. Isolines provide a measure of the skill as defined by equation (4) from *Taylor* [2001]. Blue squares compare the 7 day-averaged simulated and observed (AVISO) Sea Level at the equator (86°W), and at several coastal positions (5°S, 15°S, 25°S). Colored circles provide a comparison with the monthly SST measured by IMARPE at five piers (Paita (5.06°S), Chicama (7.7°S), Chimbote (9.08°S), Callao (12.06°S), and Pisco (13.8°S)). The black star compares PC1-SSTA time series from the EOF analysis of TMI-OI data and ROMS^{CR} outputs. Note that TMI-OI-PC1 has been shifted forward by 4 days (see Appendix A for details). (c) Coastal (0.5° coastal band averaged) Surface Vertical Thermal Gradient (SVTG, defined as the difference between the SST and the temperature at 50 m depth, blue, left scale in °C/m) and Mixed-Layer Depth (MLD, red, right scale in meters) averaged between 16°S and 8°S for ROMS^{CR} outputs (plain lines) and the CARS^{2009} climatology (dashed lines). Gray shading emphasizes the July to October season.

As a complementary validation of the subsurface mean state, Figure A3a provides a validation of the mean position of the Peruvian coastal thermocline, identified as the mean position of the 15°C isotherm averaged within a 1° coastal band (d15). ROMS^{CR} captures accurately the shallowing of the thermocline while moving southward, also in very good agreement with the mean d15 estimations using CARS^{2009} climatology. Model/observations discrepancies do not exceed 5 m in the northern Peru (0–7°S), and 15 m around 12°S. Similar discrepancies between model and the IMARPE data are found in *Dewitte et al*. [2012].

The overall comparison of ROMS^{CR} simulated mean state is encouraging to further investigate the intraseasonal coastal variability in this model configuration, in particular regarding the mean vertical stratification that is influential on the Coastal Trapped Wave characteristics. The following subsection is devoted to this issue.

A3. Variability

First, as an overall estimate of the realism of the ROMS^{CR} simulated variability, Figure A3b provides a Taylor diagram [*Taylor*, 2001], which includes various indices. The most relevant for the present study are those associated with the coastal variability of temperature and the connection with the linear equatorial dynamics, as captured by the sea level variability. In this polar plot, the azimuthal angle provides a measure of the correlation (R) between simulated and observed time series. The radial distance from the origin (r) to any point is the ratio of the model Root Mean Square (RMS) to that of the observations. The observed point, referred to as OBS and marked with a red strikethrough circle is located at (R = 1; r = 1; red circle). The distance from any point to OBF is equal to the normalized error (ratio of the RMS difference between model and observations to the RMS of the observations).

The model Sea Level Anomalies (SLA, computed with respect to the average value over the 2000–2008 period) is evaluated against the AVISO data. The latter are obtained from Ocean Topography Experiment TOPEX/Poseidon/Jason and European Remote Sensing Satellite ERS-1/2 data sets as weekly maps of Sea

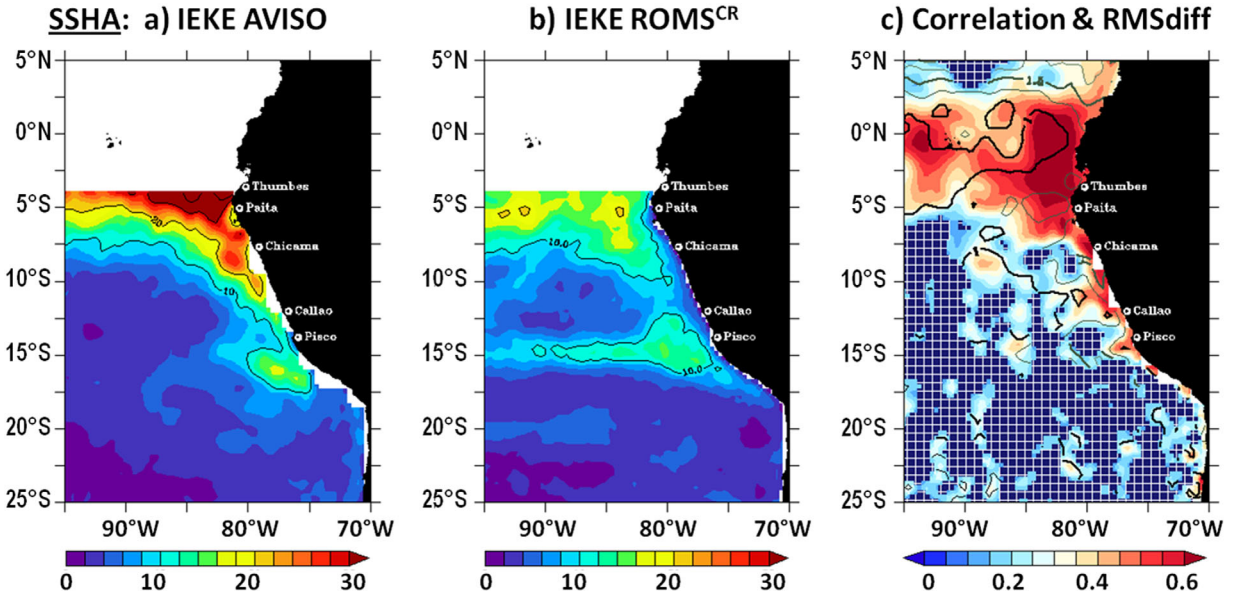

Figure A4. Maps of mean surface Intraseasonal (40–90 days) Eddy Kinetic Energy (IEKE) computed from 7 day-averaged intraseasonal sea level pressure gradients over the 2000–2008 period for (a) AVISO data and (b) ROMS^{CR} simulation. Unit is cm^2 s^{-2}. (c) Map of correlation (color shading) and RMS differences (contours) between 7 day-averaged intraseasonal sea level anomalies from ROMS^{CR} simulation and AVISO data. Blue square patterns denote non-significant correlations (95% confidence level [*Sciremammano*, 1979]). Unit of RMS is cm.

Level Anomalies (SLA) on a 1/3° Mercator grid (*Ducet et al*. [2000]—http://www.aviso.oceanobs.com). Model and data are compared at some key locations: at the equator (86°W) and southward along the Peruvian coast at 5°S, 15°S, and 25°S. The results show that ROMS^{CR} SLA is in good agreement with the observations. The agreement between model and observation is high at (0°N, 86°W), and then weakens along with the southward propagation and dissipation of the Coastal Trapped Waves. This either traduces model deficiencies or biases in the satellite observations near the coast due to the contamination of the radar signal by lands and inappropriate tropospheric corrections [*Dussurget et al*., 2011].

We then compare the monthly SST Anomalies (SSTA computed with respect to the mean over 2000–2008 period) from the IMARPE coastal stations located at Païta (5.06°S), Chicama (7.7°S), Chimbote (9.08°S), Callao (12,06°S), and Pisco (13,8°S), with equivalent ROMS^{CR} simulated time series. As model and in situ data both exhibit a marked seasonal signal (in phase with each other), with peak values in Austral summer, the results indicate a fair agreement with good level of variability and significant linear correlation coefficient in particular at Chicama, Chimbote, and Pisco. Discrepancies can be attributed to the model configuration, in particular to the spatial resolution that is too coarse to resolve the near-shore processes measured at the pier locations. Concerning the mean bias between model SST and coastal piers observed SST, the overestimated wind stress forcing near the coast (due to extrapolation of QuikSCAT data) leads to cooler than observed SST, in particular in Boreal winter, in agreement with Figure A1b.

In summary, Figure A3b indicates that over the 2000–2008 period, the model configuration is rather realistic near the coast. This suggests that the model has some skills in simulating the surface stratification variability. As a consistency check, the seasonal cycle of the Surface Vertical Thermal Gradient (defined as the difference between the SST and the temperature at 50 m depth) and the Mixed-Layer Depth averaged in the 100 km coastal band between 16°S and 8°S are displayed on Figure A3c for the model outputs and the observations. It shows that both amplitude and phase of the simulated surface stratification are in very good agreement with the observations. Taylor skills, as estimated from *Taylor* [2001, equation (4)], are larger than 0.99 (0.96) for SVTG (MLD).

Now we will focus on the evaluation of ROMS^{CR} skill in simulating the variability within the intraseasonal time scales (40–90 days). The Intraseasonal Eddy Kinetic Energy (IEKE) is first diagnosed (Figures A4a and A4b) in order to estimate the realism of the intraseasonal mesoscale activity in the model. Note that usually the total mean EKE is considered for validation purpose. Here since our interest is on the intraseasonal variability, we consider the IEKE and compare it to estimations based on satellite altimetry (AVISO data). Note also that, since there

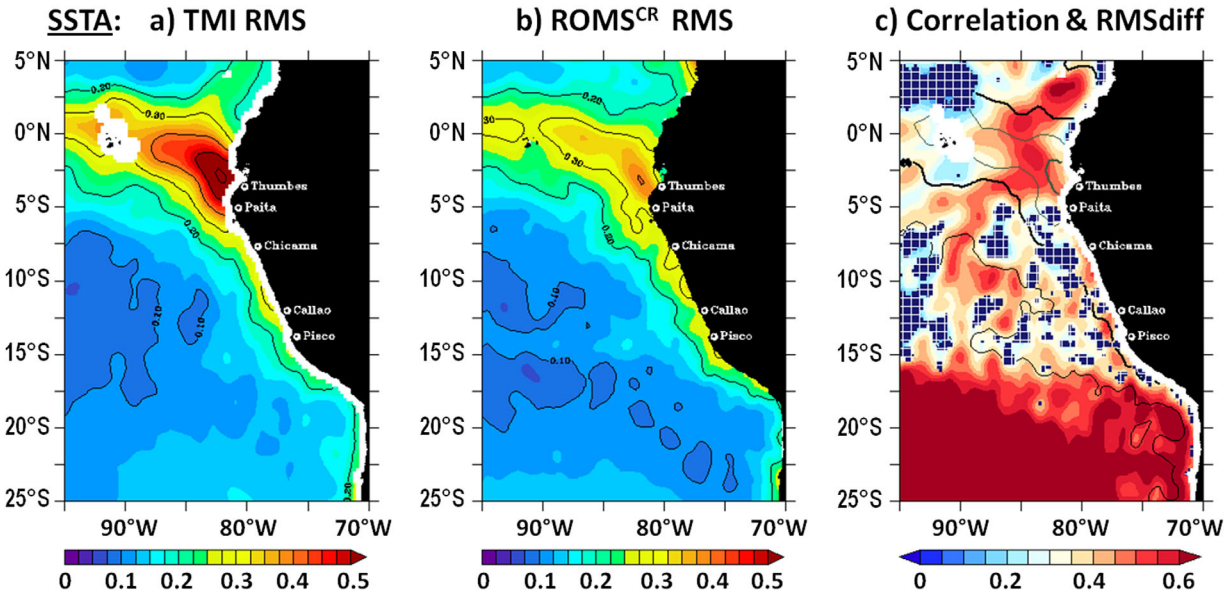

Figure A5. Analysis of daily Sea Surface Temperature intraseasonal (40–90 days) Anomalies (SSTA) over the 2000–2008 period: Map of variability (RMS) for (a) TMI-OI data and (b) ROMS^{CR} simulation. (c) Map of correlation (color shading) and RMS differences (contours) between observed and simulated SSTA. Blue square patterns denote non-significant correlations (95% confidence level [*Sciremammano*, 1979]). Unit is °C.

is no data assimilation in the model, observed and simulated eddies are not expected to agree in their individual features. However, their statistical characteristics (IEKE distribution and intensity) are comparable in both the model and the observations, which indirectly reflects a realistic vertical current structure variability and associated intraseasonal eddy activity. Although model and altimetry have different spatial resolutions, both products show local maxima of EKE near the equator and along the coast of Peru down to 16°S with a similar spatial pattern (the spatial correlation is 0.81). A notable discrepancy between the model solution and the observations is the underestimated IEKE north of 7°S: ∼15 cm^2 s^{-2} in the model versus ∼30 cm^2 s^{-2} based on satellite data. This is likely due to the weaker than observed equatorial variability in the SODA model. Another remarkable difference consists in a significantly smaller IEKE in the first ∼100 km in the model simulation relative to the observations, a feature that was also mentioned by previous studies [*Montes et al.*, 2010; *Colas et al.*, 2011].

Focusing now on the intraseasonal Sea Level Anomalies (SLA), Figure A4c displays the correlation and RMS differences between model and observations (weekly altimetric AVISO data). The agreement between model and observations is statistically significant along the equatorial wave guide and its coastal extension, with correlation values larger than 0.5 and RMS differences lower than 1 cm. Note that the agreement between model and observations decreases southward along the coast (see also Figure A3). Further offshore, the lack of agreement between model and observations (correlation is not significant and RMS differences are of the order of the RMS) has to be attributed to the mesoscale activity (see Figures A4a and A4b). Although the model IEKE is realistic (Figure A4), since there is no data assimilation in the model, simulated and observed eddies are not collocated. This results in noisy features at the time and spatial scales of the eddies themselves and explains the low agreement of SLA where eddy activity is the largest. In order to filter out the noisy features associated with the mesoscale activity, the data are averaged over a coastal fringe of 100 km width between 16°S and 8°S. In that case, the correlation between observation and model reaches 0.61 (with a RMS difference smaller than 0.9 cm).

We now focus on the comparison between model and observations (TMI-OI) for the intraseasonal SST Anomalies (SSTA). First, a statistical comparison (Figure A5) indicates that the ROMS^{CR} and daily TMI-OI data share the same level of intraseasonal variability, with a comparable spatial pattern (spatial correlation of RMS maps is 0.90), in particular off Peru, the region of interest in this study. However, in this region, the correlation between model and observations is not significant, and the RMS difference remains of the order of the RMS (Figure A6c). As mentioned above, this discrepancy between model and observations is due to the signature of eddies on SSTAs: ROMS^{CR} eddies are not necessarily collocated with those observed by TMI-OI. Also TMI-OI is a gridded product with correlation scales of 4 days and 100 km, which tends to smooth the mesoscale signature on SST. Such interpolation procedure was not applied to the model outputs. As a

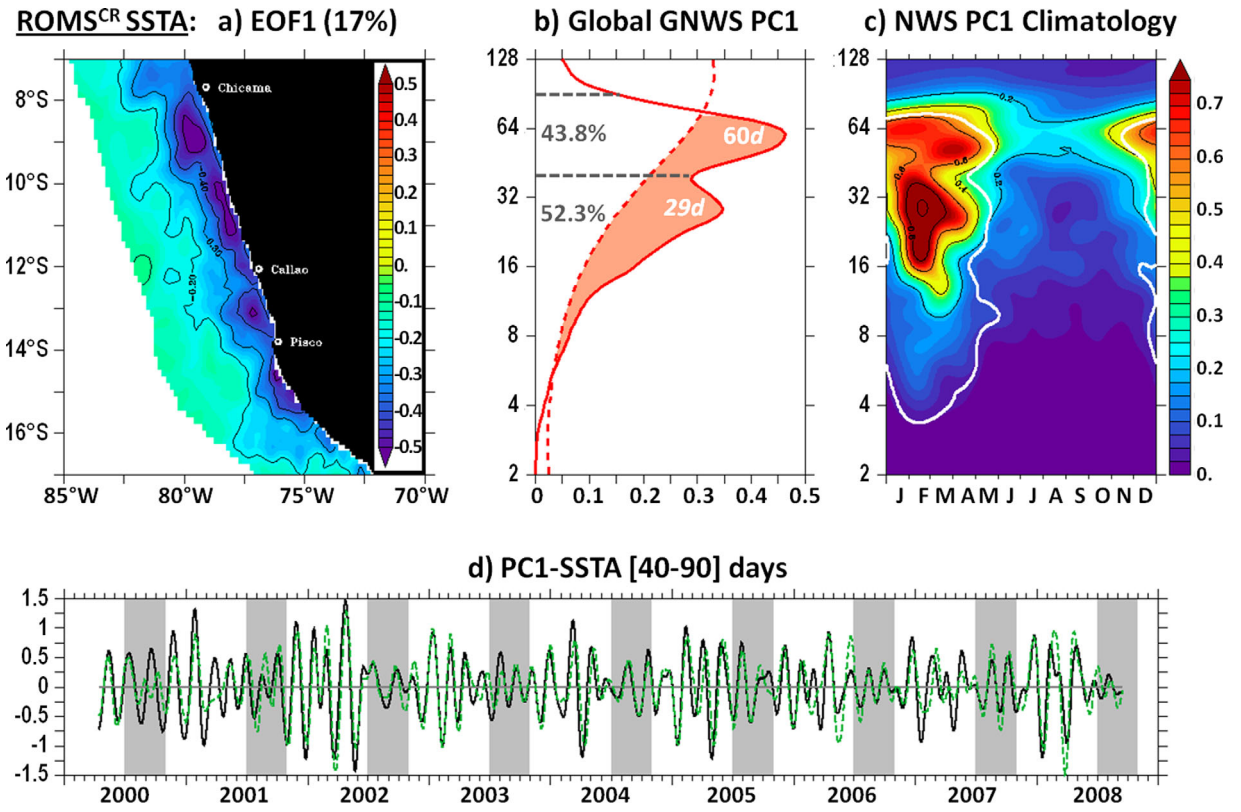

Figure A6. (top) Maps are same as Figure 1 but for ROMS^{CR} SST subseasonal anomalies. (bottom) Intraseasonal band-pass filtered PC1-SSTA (40–90 days) for ROMS^{CR} (black plain line) and TMI-OI (green dashed line). Note that TMI-OI-PC1 has been shifted forward by 4 days (see Appendix A for details). Gray vertical bands show the July to October season.

consistency check, we estimated the level of agreement between model and observations of the SSTA averaged in the 200 km coastal band between 16°S and 8°S. The correlation then reaches 0.72, while the RMS difference remains lower than 0.2°C. This indicates that the model has some skills in simulating the SST intraseasonal variability near the coast.

The agreement between model and observations is further assessed based on an EOF analysis of the model intraseasonal SSTA within a 5° wide coastal fringe between 17°S and 7°S, which allows extracting the SST variability associated with the upwelling variability. Figure A6 displays the ROMS^{CR} dominant pattern of variability of the SSTAs at subseasonal time scales off central Peru. The comparison between Figure A6 and Figure 1 that shows the results of EOF analysis for the observed SSTA indicates that the model captures the main characteristics of the dominant mode of intraseasonal SSTAs off central Peru, that is: maximum variability confined within 200 km from the coast (Figure A6a), two regimes of variability peaking at 29 and 60 days and accounting respectively for 52% and 44% of the total power of the PC1-SSTA spectrum (Figure A6b), and a marked seasonal dependence of the variability peak variance (Figure A6c). Note that this dominant mode explains 17% of the ROMS^{CR} subseasonal variance, against 33% for the TMI-OI data. This has to be attributed to the larger mesoscale activity in ROMS^{CR} compared to TMI-OI data that does not project onto the spatial pattern of EOF1. Applying a low-pass spatial filter (binning within a 100 km radius) to the model outputs allows for increasing the averaged explained variance up to 29.5%, which is in better agreement with the observations. Note that, besides the inherent limitations of the model, differences between model and observations also originate from the consideration of the SST data within the coastal masking zone of the TMI-OI data set for the model result (not shown).

Figure A6d displays the PC1-SSTA time series for ROMS^{CR} (black plain line) and TMI-OI (green dashed line) filtered at intraseasonal time scales. The time series are lagged in time, ROMS^{CR} PC1-SSTA leading TMI-OI by 4 days. This is attributed to the extended masking of the TMI-OI data near the coast, which results in an offshore extension of the EOF1 spatial pattern more developed for TMI-OI analysis than for the model. Thus, the TMI-OI EOF1 corresponds to a 4 day delayed phase in the upwelling sequence (cf. section 5.2) compared to the EOF

pattern captured in ROMS^{CR} outputs that is more coastal. Correlation and RMS difference between model and observations are, respectively, 0.88 and 0.25°C for a lag of 4 days with the model PC1 leading. This corresponds to a high score in the Tailor diagram (black star in Figure A3b in Appendix A) of 0.93 that emphasizes the agreement between model and observations in simulating the intraseasonal SST variability off central Peru.

Overall, the comparison between model and observations indicates that the model is skilfull in simulating most aspects of the mean state and intraseasonal variability, which provides confidence for using the model for diagnostic studies and sensitivity tests to boundary forcings.

Acknowledgments

We would like to thank the CNES (OSTST project EBUS-SOUTH, OSTST project MODOKALT) and ESA (project OceanFlux) for financial support. TMI-OI data are produced by Remote Sensing Systems and sponsored by the NASA Earth Science MEaSUREs DISCOVER Project. Wind stress data were obtained from the Centre de Recherche et d'Exploitation Satellitaire (CERSAT), at IFREMER, Plouzané (France). We are grateful to B. Giese from Texas A&M University for providing the SODA data. We are thankful to the DSI/IRD for supporting the SPIRALES project dedicated to the implementation of a cluster at IMARPE (P.I: B. Dewitte) over which the model configuration used in this study was developed and most simulations were performed. Some were also performed on the CALMIP computer at University Paul Sabatier (Toulouse, France, CALMIP project 1044). The model grid, forcing, and initial conditions were built using the ROMSTOOLS package [*Penven et al.*, 2008]. The authors wish to acknowledge use of the Ferret program (NOAA PMEL, http://ferret.pmel.noaa.gov) for analysis and graphics in this paper. The three anonymous reviewers are thanked for their constructive comments.

References

Bakun, A. (1990), Global climate change and intensification of coastal ocean upwelling, *Science*, *247*, 198–201.

Belmadani, A., V. Echevin, B. Dewitte, and F. Colas (2012), Equatorially forced intraseasonal propagations along the Peru-Chile coast and their relation with the nearshore eddy activity in 1992–2000: A modelling study, *J. Geophys. Res.*, *117*, C04025, doi:10.1029/2011JC007848.

Brink, K. H. (1982), A comparison of long coastal trapped wave theory with observations off Peru, *J. Phys. Oceanogr.*, *12*, 897–913.

Brochier, T., V. Echevin, J. Tam, A. Chaigneau, K. Goubanova, and A. Bertrand (2013), Climate change scenarios experiments predict a future reduction in small pelagic fish recruitment in the Humboldt Current system, *Global Change Biology*, *19*(6), 1841–1853, doi:10.1111/gcb.12184.

Bromwich, D. H., R. L. Fogt, K. E. Hodges, and J. E. Walsh (2006), A tropospheric assessment of the ERA-40, NCEP, and JRA-25 global reanalyses in the polar regions, *J. Geophys. Res.*, *112*, D10111, doi:10.1029/2006JD007859.

Camayo, R., and E. J. D. Campos (2006), Application of wavelet transform in the study of coastal trapped waves off the west coast of South America, *Geophys. Res. Lett.*, *33*, L22601, doi:10.1029/2006GL026395.

Cambon, G., K. Goubanova, P. Marchesiello, B. Dewitte, S. Illig, and V. Echevin (2013), Assessing the impact of downscaled winds on a regional ocean model simulation of the Humboldt system, *Ocean Modell.*, *65*, 11–24.

Capet, X. J., P. Marchesiello, and J. C. McWilliams (2004), Upwelling response to coastal wind profiles, *Geophys. Res. Lett.*, *31*, L13311, doi:10.1029/2004GL020123.

Carr, M.-E. (2002), Estimation of potential productivity in eastern boundary currents using remote sensing, *Deep Sea Res., Part II*, *49*, 59–80.

Carton, J. A., and B. S. Giese (2008), A reanalysis of ocean climate using simple ocean data assimilation (SODA), *Mon. Weather Rev.*, *136*, 2999–3017, doi:10.1175/2007MWR1978.1.

Carton, J. A., G. Chepurin, and X. Cao (2000), A simple ocean data assimilation analysis of the global upper ocean 1950–95. Part I: Methodology, *J. Phys. Oceanogr.*, *30*, 294–309.

Centre ERS d'Archivage, de Traitement (CERSAT) (2002), Mean wind fields (MWF product) user manual, 1, QuikSCAT, *Rep. C2-MUT-W-04-IF*, Ifremer, Plouzane, France.

Clarke, A., and R. Ahmed (1999), Dynamics of remotely forced intraseasonal oscillations off the western coast of South America, *J. Phys. Oceanogr.*, *29*, 240–258.

Clarke, A. J., and C. Shi (1991), Critical frequencies at ocean boundaries, *J. Geophys. Res.*, *96*, 10,731–10,738, doi:10.1029/91JC00933.

Colas, F., X. Capet, J. C. McWilliams, and A. Shchepetkin (2008), 1997–98 El Niño off Peru: A numerical study, *Prog. Oceanogr.*, *79*, 138–155, doi:10.1016/j.pocean.2008.10.015.

Colas, F., J. C. McWilliams, X. Capet, and J. Kurian (2011), Heat balance and eddies in the Peru–Chile current system, *Clim Dyn*, *39*, 509–529, doi:10.1007/s00382-011-1170-6.

Debreu, L., P. Marchesiello, P. Penven, and G. Cambon (2012), Two-way nesting in split-explicit ocean models: Algorithms, implementation and validation, *Ocean Modell.*, *49–50*, 1–21.

Demarcq, H., and V. Faure (2000), Coastal upwelling and associated retention indices derived from satellite SST. Application to *Octopus vulgaris* recruitment, *Oceanol. Acta*, *23*, 391–408.

Dewitte, B., S. Illig, L. Parent, Y. duPenhoat, L. Gourdeau, and J. Verron (2003), Tropical Pacific baroclinic mode contribution and associated long waves for the 1994–1999 period from an assimilation experiment with altimetric data, *J. Geophys. Res.*, *108*(C4), 3121, doi:10.1029/2002JC001362.

Dewitte, B., S. Purca, S. Illig, L. Renault, and B. Giese (2008a), Low frequency modulation of the intraseasonal equatorial Kelvin wave activity in the Pacific Ocean from SODA: 1958–2001, *J. Clim.*, *21*, 6060–6069.

Dewitte, B., M. Ramos, V. Echevin, O. Pizarro, and Y. duPenhoat (2008b), Vertical structure variability in a seasonal simulation of a medium-resolution regional model simulation of the South Eastern Pacific, *Prog. Oceanogr.*, *79*, 120–137.

Dewitte, B., S. Illig, L. Renault, K. Goubanova, K. Takahashi, D. Gushchina, K. Mosquera, and S. Purca (2011), Modes of covariability between sea surface temperature and wind stress intraseasonal anomalies along the coast of Peru from satellite observations (2000–2008), *J. Geophys. Res.*, *116*, C04028, doi:10.1029/2010JC006495.

Dewitte, B., J. Vazquez-Cuervo, K. Goubanova, S. Illig, K. Takahashi, G. Cambon, S. Purca, 1107 D. Correa, D. Gutierrez, A. Sifeddine, and L. Ortlieb (2012), Change in El Niño flavours over 1958–2008: Implications for the long-term trend of the upwelling off Peru, *Deep Sea Res., Part II, 77–80*, 143–156, doi:10.1016/j.dsr2.2012.04.011.

Ducet, N., P. Y. Le Traon, and G. Reverdin (2000), Global high-resolution mapping of ocean circulation from the combination of T/P and ERS-1/2, *J. Geophys. Res.*, *105*, 19,477–19,498, doi:10.1029/2000JC900063.

Duchon, C. (1979), Lanczos filtering in one and two dimensions, *J. Appl. Meteorol.*, *18*, 1016–1022.

Dufois, F., P. Penven, C. P. Whittle, and J. Veitch (2012), On the warm nearshore bias in Pathfinder monthly SST products over Eastern Boundary Upwelling Systems, *Ocean Modelling*, *47*, 113–118, doi:10.1016/j.ocemod.2012.01.007.

Dussurget, R., F. Birol, R. Morrow, and P. De Mey (2011), Fine resolution altimetry data for a regional application in the bay of biscay marine geodesy, *Mar. Geol.*, *34*, 447–476, doi:10.1080/01490419.2011.584835.

Echevin, V., K. Goubanova, B. Dewitte, and A. Belmadani (2012), Sensitivity of the Humboldt Current system to global warming: A downscaling experiment of the IPSL-CM4 model, *Clim. Dyn.*, *38*(3-4), 761–774, doi:10.1007/s00382-011-1085-2.

Enfield, D. B. (1987), The intraseasonal oscillation in Eastern Pacific sea levels: How is it forced?, *J. Phys. Oceanogr.*, *17*, 1860–1876.

Enfield, D. B., M. P. Cornejo-Rodriguez, R. L. Smith, and P. A. Newberger (1987), The equatorial source of propagating variability along the Peru coast during the 1982–1983 El Niño, *J. Geophys. Res.*, *92*, 14,335–14,346, doi:10.1029/JC092iC13p14335.

Flores, R., J. Tenorio, and N. Dominguez (2010), Variaciones de la extensión Sur de la Corriente Cromwell frente al Perú entre los 3°-14°S, *Bol. Inst. del Mar del Perú*, *24*(1–2), 45–55.
Fox-Kemper, B., and R. Ferrari (2008), Parameterization of mixed layereddies. PartII: Prognosis and impact, *J. Phys. Oceanogr.*, *38*, 1166–1179.
Garreaud, R., and R. Muñoz (2005), The low-level jet off the subtropical west coast of South America: Structure and variability, *Mon. Weather Rev.*, *133*, 2246–2261, doi:10.1175/MWR2972.1.
Gentemann, C., C. J. Donlon, A. Stuart-Menteth, and F. J. Wentz (2003), Diurnal signals in satellite sea surface temperature measurements, *Geophys. Res. Lett.*, *30*(3), 1140, doi:10.1029/2002GL016291.
Gentemann, C., F. J. Wentz, M. Brewer, K. Hiburn, and D. Smith (2010), Passive microwave remote sensing of the ocean: An overview, in *Oceanography From Space, Revisited*, edited by V. Barale, J. Gower, and L. Alberotanza, pp. 13–33, Springer, Heidelberg, Germany.
Goubanova, K., V. Echevin, B. Dewitte, F. Codron, K. Takahashi, P. Terray, and M. Vrac (2011), Statistical downscaling of sea-surface wind over the Peru-Chile upwelling region: diagnosing the impact of climate change from the IPSL-CM4 model, *Clim. Dyn.*, *36*(7-8), 1365–1378, doi:10.1007/s00382-010-0824-0.
Goubanova, K., S. Illig, E. Machu, V. Garçon, and B. Dewitte (2013), SST subseasonal variability in the Benguela upwelling system as inferred from satellite observations (2000–2008), *J. Geophys. Res. Oceans*, *118*, 4092–4110, doi:10.1002/jgrc.20287.
Gutiérrez, D., et al. (2011), Coastal cooling and increased productivity in the main upwelling zone off Peru since the mid-twentieth century, *Geophys. Res. Lett.*, *38*, L07603, doi:10.1029/2010GL046324.
Hayashi, Y. (1982), Space-time spectral analysis and its applications to atmospheric waves, *J. Meteorol. Soc. Jpn.*, *60*, 156–171.
Hormazabal, S., G. Shaffer, and O. Pizarro (2002), Tropical Pacific control of intraseasonal oscillations off Chile by way of oceanic and atmospheric pathways, *Geophys. Res. Lett.*, *29*(6), 1081, doi:10.1029/2001GL013481.
Huyer, A., R. L. Smith, and T. Paluszkiewicz (1987), Coastal upwelling off Peru during normal and El Niño times, *J. Geophys. Res.*, *92*, 14,297–14,307, doi:10.1029/JC092iC13p14297.
Huyer, A., M. Knoll, T. Paluszkiewic, and R. L. Smith (1991), The Peru Undercurrent: A study of variability, *Deep Sea Res., Part A*, *38*, S247–S271.
Juliá, C., D. A. Rahn, and J. A. Rutllant (2012), Assessing the influence of the MJO on strong precipitation events in subtropical, semi-arid north-central Chile (30°S), *J. Clim.*, *25*, 7003–7013.
Kondo, J. (1975), Air-sea bulk transfer coefficients in diabatic conditions, *Boundary Layer Meteorol.*, *9*, 91–112.
Kummerow, C., et al. (2000), The status of the tropical rainfall measuring mission (TRMM) after two years in orbit, *J. Appl. Meteorol.*, *39*, 1965–1982.
Large, W., J. McWilliams, and S. Doney (1994), Oceanic vertical mixing: A review and a model with a nonlocal boundary layer parameterization, *Rev. Geophys.*, *32*, 363–403.
Marchesiello, P., and P. Estrade (2010), Upwelling limitation by geostrophic onshore flow, *J. Mar. Res.*, *68*, 37–62.
Marchesiello, P., J. C. McWilliams, and A. Shchepetkin (2001), Open boundary conditions for long-term integration of regional oceanic models, *Ocean Modell.*, *3*, 1–20.
Marchesiello, P., J. McWilliams, and A. Shchepetkin (2003), Equilibrium structure and dynamics of the California current system, *J. Phys. Oceanogr.*, *33*, 753–783.
Mechoso, C. R., et al. (2013), Ocean-cloud-atmosphere-land interactions in the Southeastern Pacific: The VOCALS program, *Bull. Am. Meteorol. Soc.*, *95*, 357–375, doi:10.1175/BAMS-D-11-00246.1.
Menkes, C. E. R., J. G. Vialard, S. C. Kennan, J. P. Boulanger, and G. V. Madec (2006), A modeling study of the impact of tropical instability waves on the heat budget of the eastern equatorial Pacific, *J. Phys. Oceanogr.*, *36*, 847–865.
Montecinos, A., and F. Gomez (2010), ENSO modulation of the upwelling season off southern-Central Chile, *Geophys. Res. Lett.*, *33*, L02708, doi:10.1029/2009GL041739.
Montes, I., F. Colas, X. Capet, and W. Schneider (2010), On the pathways of the equatorial subsurface currents in the eastern equatorial Pacific and their contributions to the Peru-Chile Undercurrent, *J. Geophys. Res.*, *115*, C09003, doi:10.1029/2009JC005710.
Penven, P., V. Echevin, J. Pasapera, F. Colas, and J. Tam (2005), Average circulation, seasonal cycle, and mesoscale dynamics of the Peru Current System: A modeling approach, *J. Geophys. Res.*, *110*, C10021, doi:10.1029/2005JC002945.
Penven, P., L. Debreu, P. Marchesiello, and J. C. McWilliams (2006), Evaluation and application of the ROMS 1-way embedding procedure to the central California upwelling system, *Ocean Modell.*, *12*, 157–187.
Penven, P., P. Marchesiello, L. Debreu, and J. Lefevre (2008), Software tools for pre- and post-processing of oceanic regional simulations, *Environ. Model. Software*, *23*, 660–662.
Pizarro, O., A. J. Clarke, and S. Van Gorder (2001), El Niño sea level and currents along the South American coast: Comparison of observations with theory, *J. Phys. Oceanogr.*, *31*(7), 1891–1903.
Pizarro, O., G. Shaffer, B. Dewitte, and M. Ramos (2002), Dynamics of seasonal and interannual variability of the Peru–Chile Undercurrent, *Geophys. Res. Lett.*, *29*(12), 1581, doi:10.1029/2002GL014790.
Rahn, D. A. (2012), Influence of large scale oscillations on upwelling-favorable coastal wind off central Chile, *J. Geophys. Res.*, *117*, D19114, doi:10.1029/2012JD018016.
Ramos, M., O. Pizarro, L. Bravo, and B. Dewitte (2006), Seasonal variability of the permanent thermocline off northern Chile, *Geophys. Res. Lett.*, *33*, L09608, doi:10.1029/2006GL025882.
Ramos, M., B. Dewitte, O. Pizarro, and G. Garric (2008), Vertical propagation of extratropical Rossby waves during the 1997–1998 El Niño off the west coast of South America in a medium-resolution OGCM simulation, *J. Geophys. Res.*, *113*, C08041, doi:10.1029/2007JC004681.
Renault, L., B. Dewitte, M. Falvey, R. Garreaud, V. Echevin, and F. Bonjean (2009), Impact of atmospheric coastal jets on SST off central Chile from satellite observations (2000–2007), *J. Geophys. Res.*, *114*, C08006, doi:10.1029/2008JC005083.
Renault, L., B. Dewitte, P. Marchesiello, S. Illig, V. Echevin, G. Cambon, M. Ramos, O. Astudillo, P. Minnis, and J. K. Ayers (2012), Upwelling response to atmospheric coastal jets off Central Chile: A modeling study of the October 2000 event, *J. Geophys. Res.*, *117*, C02030, doi:10.1029/2011JC007446.
Reynolds, R. W., and T. M. Smith (1994), Improved global sea surface temperature analyses using optimum interpolation, *J. Clim.*, *7*, 929–948.
Ridgway, K. R., J. R. Dunn, and J. L. Wilkin (2002), Ocean interpolation by four-dimensional least squares—Application to the waters around Australia, *J. Atmos. Oceanic Technol.*, *19*(9), 1357–1375.
Schweiger, A. J., R. W. Lindsay, S. Vavrus, and J. Francis (2008), Relationships between Arctic sea ice and clouds during autumn, *J. Clim.*, *21*, 4799–4810.
Sciremammano, F. (1979), A suggestion for the presentation of correlations and their significance levels, *J. Phys. Oceanogr.*, *9*, 1273–1276.

Shaffer, G., O. Pizarro, L. Djurfeldt, S. Salinas, and J. Rutllant (1997), Circulation and low-frequency variability near the Chilean coast: Remotely forced fluctuations during the 1991–1992 El Niño, *J. Phys. Oceanogr.*, *27*, 217–235.

Shchepetkin, A. F., and J. C. McWilliams (1998), Quasi-monotone advection schemes based on explicit locally adaptive dissipation, *Mon. Weather Rev.*, *126*, 1541–1580.

Shchepetkin, A. F., and J. C. McWilliams (2005), The regional oceanic modeling system: A split-explicit, free-surface, topography following-coordinate ocean model, *Ocean Modell.*, *9*, 347–404, doi:10.1016/j.ocemod.2004.08.002.

Smith, R., J. Dukowicz, and R. Malone (1992), Parallel ocean general circulation modeling, *Physica D.*, *60*, 38–61.

Spillane, M. C., D. B. Enfield, and J. S. Allen (1987), Intraseasonal oscillations in sea level along the west coast of the Americas, *J. Phys. Oceanogr.*, *17*, 313–325.

Strub, P. T., J. M. Mesias, V. Montecino, J. Rutllant, and S. Salinas (1998), Coastal ocean circulation off western South America, in *The Sea*, vol. 11, edited by A. R. Robinson and K. H. Brink, pp. 273–314, John Wiley, Hoboken, N. J.

Taylor, K. E. (2001), Summarizing multiple aspects of model performance in a single diagram, *J. Geophys. Res.*, *106*, 7183–7192.

Torrence, C., and G. P. Compo (1998), A practical guide to wavelet analysis, *Bull. Am. Meteorol. Soc.*, *79*, 61–78.

Toumazou, V., and J.-F. Cretaux (2001), Using a Lanczos Eigensolver in the computation of empirical orthogonal functions, *Mon. Weather Rev.*, *129*, 1243–1250.

Uppala, S. M., et al. (2005), The ERA-40 re-analysis, *Q. J. R. Meteorol. Soc.*, *131*, 2961–3012.

Vega, A., Y. duPenhoat, B. Dewitte, and O. Pizarro (2003), Equatorial forcing of interannual Rossby waves in the South eastern Pacific, *Geophys. Res. Lett.*, *30*(5), 1197, doi:10.1029/2002GL015886.

Wentz, F. J., C. L. Gentemann, D. K. Smith, and D. B. Chelton (2000), Satellite Measurements of sea surface temperature through clouds, *Science*, *288*(5467), 847–850.

Xie, S. P., T. Miyama, Y. Q. Wang, H. M. Xu, S. P. de Szoeke, R. J. O. Small, K. J. Richards, T. Mochizuki, and T. Awaji (2007), A regional ocean-atmosphere model for eastern Pacific climate: Toward reducing tropical biases, *J. Clim.*, *20*, 1504–1522.